# LARGE DISPLACEMENT ANALYSIS OF SHELL STRUCTURES USING THE ABSOLUTE NODAL **COORDINATE FORMULATION**

**Mechanical Engineering**
Technical Report ME-TR-6

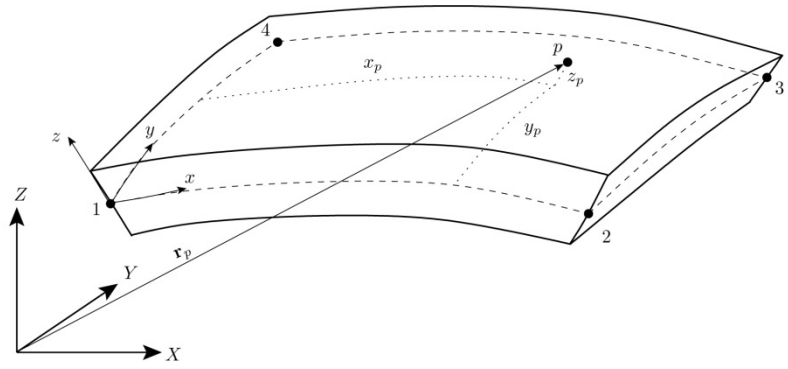


AARHUS
UNIVERSITY
DEPARTMENT OF ENGINEERING

# DATA SHEET

**Title:** Large Displacement Analysis of Shell Structures using the Absolute Nodal Coordinate Formulation.

**Subtitle:** Mechanical Engineering
**Series title and no.:** Technical report ME-TR-6

**Author:** Per Hyldahl
Department of Engineering – Mechanical Engineering, Aarhus University

**Internet version:** The report is available in electronic format (pdf) at the Department of Engineering website http://www.eng.au.dk.

**Publisher:** Aarhus University©
**URL:** http://www.eng.au.dk

**Year of publication:** 2013 Pages: 38
**Editing completed:** July 2013

**Abstract:** This report will review and discuss thin rectangular ANCF shell elements. First, a thorough review of the kinematic descriptions used in the current thin rectangular ANCF shells is given. This review will also contain a derivation of the equations of motion. Subsequently, a novel ANCF shell finite element with dynamic mesh properties is reviewed. This element is characterized by being able to change element size during transient simulation. The following chapter contains a preliminary study of the kinematics and numerical performance of thin rectangular ANCF shell elements when used in a curved and distorted mesh. A more general comparison of current element formulations is also performed. The results from the ANCF elements are compared to solutions obtained using a traditional commercial finite element code. At the end, the content of this report is summed up in a conclusion, and the outline of future work is presented.

**Keywords:** Absolute Nodal Coordinate Formulation, ANCF, Multibody Dynamics, Finite Element Method, Large Displacements, Arbitrary Lagrange Euler, ALE, Structural Dynamics

**Supervisor:** Ole Balling

**Please cite as:** Per Hyldahl, 2013. Large Displacement Analysis of Shell Structures using the Absolute Nodal Coordinate Formulation. Department of Engineering, Aarhus University. Denmark. 38 pp. - Technical report ME-TR-6

**Cover image:** Per Hyldahl

**ISSN:** 2245-4594

# LARGE DISPLACEMENT ANALYSIS OF SHELL STRUCTURES USING THE ABSOLUTE NODAL COORDINATE FORMULATION

Per Hyldahl

Aarhus University, Department of Engineering

**Abstract**

This report will review and discuss thin rectangular ANCF shell elements. First, a thorough review of the kinematic descriptions used in the current thin rectangular ANCF shells is given. This review will also contain a derivation of the equations of motion. Subsequently, a novel ANCF shell finite element with dynamic mesh properties is reviewed. This element is characterized by being able to change element size during transient simulation. The following chapter contains a preliminary study of the kinematics and numerical performance of thin rectangular ANCF shell elements when used in a curved and distorted mesh. A more general comparison of current element formulations is also performed. The results from the ANCF elements are compared to solutions obtained using a traditional commercial finite element code. At the end, the content of this report is summed up in a conclusion, and the outline of future work is presented.

# Nomenclature

## Matrix and vector variables

| | |
|---|---|
| $\mathbf{r}$ | Position vector of an arbitrary point on an ANCF element |
| $\mathbf{r}_i$ | Position vector of node $i$ |
| $\mathbf{q}$ | Vector of generalized coordinates for an element |
| $\mathbf{N}$ | Matrix of shape functions |
| $\mathbf{M}$ | Mass matrix |
| $\mathbf{E}$ | Constitutive matrix |
| $\mathbf{Q}_e$ | Vector of elastic forces |
| $\mathbf{Q}_f$ | Vector of external forces |
| $\boldsymbol{\epsilon}$ | Vector of unique terms of the Green-Lagrange strain tensor |
| $\boldsymbol{\kappa}$ | Vector of unique terms of the curvature tensor |
| $\boldsymbol{\Phi}$ | Vector of algebraic constraint equations |
| $\boldsymbol{\lambda}$ | Vector of Lagrange multipliers |

## Latin variables

| | |
|---|---|
| $X, Y, Z$ | Global coordinates |
| $x, y, z$ | Local element coordinates |
| $m_i, n_i$ | Local material coordinates |
| $L, W$ | Element length and width, respectively |
| $t$ | Element thickness |
| $U$ | Elastic energy |
| $E$ | Young's modulus |

## Greek variables

| | |
|---|---|
| $\xi, \eta$ | Isoparametric mapping parameters |
| $\alpha, \beta$ | Tensor notation index counters. Can take the values 1 and 2. |
| $\nu$ | Poisson ratio |
| $\epsilon_{\alpha\beta}$ | Green-Lagrange Strain Tensor |
| $\kappa_{\alpha\beta}$ | Geometrical curvature tensor |

## Mathematical operators

| | |
|---|---|
| $[\cdot]^T$ | Matrix transpose |
| $[\cdot]^{-1}$ | Matrix inverse |
| $\delta[\cdot]$ | Virtual operator |
| $\partial[\cdot]$ | Partial derivative operator |
| $\dot{[\cdot]}$ | First order time derivative |
| $\ddot{[\cdot]}$ | Second order time derivative |
| $\otimes$ | Kronecker product |

# Preface

This report is part of the qualifying exam in the PhD programme at the Graduate School of Science and Technology at Aarhus University, Denmark. It acts as a documentation for the work carried out during the first half of the PhD study. Furthermore, the report will outline of the remainder of the study.

Per Hyldahl, Aarhus, August 23, 2013

# Contents

Chapter 1

# Introduction

The design engineers of today are facing remarkable challenges, when designing new products and machines. The requirements demanded by both consumers and legislators seems to be ever increasing and products must be larger, lighter, faster, and more reliable and versatile to maintain a market leading position. Additionally, the major challenge in applying for financial support for new product investments calls for higher focus in reliable risk analysis. To comply with these demands design engineers are turning toward new and advanced methods in the design process. Exotic materials such as light weight metal alloys and fiber reinforced polymer composites are chosen to obtain light weight products, good aesthetic characteristics and/or low energy consumption both in the production, the service and decomposition phase. Advanced manufacturing processes such as rapid prototyping and robotics are used for low production cycles and customer specific products. Sophisticated simulation software is used throughout the entire design process for enhanced product insight and optimized product behavior. During the later years the combination of advanced simulation tools and increasing computational power has made it possible to simulate extreme events and perform numerous *what-if* scenarios in a virtual environment. The use of computer-aided engineering tools makes it possible to investigate the potential of any plausible design by including e.g non-linear material descriptions, Fluid-Structural Interaction (FSI) and large displacement formulations in numerical models. This has reduced the need of physical testing, leading to reduced time to market and safer and more reliable products.

Engineers must choose an appropriate analysis tool for the problem at hand when designing complex mechanical systems design. If the mechanical system is dominated by large rigid-body motion rather than deformations, multibody dynamics would be an obvious choice [Haug, 1989; Nikravesh, 1988; Shabana, 2005; Schiehlen, 1997]. Multibody dynamics is developed specifically to model the interaction between interconnected bodies when subjected to complicated loading while taking into account inertia forces due to large overall rigid body motion. This makes it possible to efficiently analyze and optimize, e.g. dynamic behavior of systems for improved load carrying capacity or performance behavior. Multibody dynamics has a proven track record of successful applications in several engineering fields, including robotics, aerospace engineering, energy industry, vehicle dynamics, bio-mechanics, and rotor dynamics.

When analyzing a mechanical system, the modeling of the kinematic coupling of bodies is an essential part. The kinematic coupling of bodies is modeled using algebraic constraint equations [Haug, 1989; Nikravesh, 1988]. These constraints are used to model idealized joints that allows for some relative motion between bodies while eliminating others. These constraint equations are in the general case highly non-linear equations that are functions of both the system configuration and time. The constraint equations can be coupled with the Newton-Euler equations leading to a set of constrained equations of motion for the

entire system. These set of equations contains both algebraic and differential terms. Due to the non-linearity of both the constraint equations and the overall motion of the system, in general, there exists no analytical closed form solution to the constrained equations of motion. This calls for efficient numerical solution techniques in order to simulate system behavior over time.

Traditionally, when using multibody dynamics, bodies have been considered rigid [Haug, 1989]. In recent years, though, the multibody approach has been expanded to incorporate deformations to enhance the results and gain detailed insight in the performance of systems where deflections will affect the dynamic behavior. Depending on the nature of the deformations several techniques can be applied [Shabana, 1997b; Wasfy and Noor, 2003]. The most widely used method is known as the Floating Frame of Reference formulation (FFRF). In the FFRF, the displacement of a deformable body is divided into large overall motion of a local reference frame fixed to the body and deformations expressed with respect to this frame. Depending on the shape of the body, the local body deformations can be calculated in several ways [Shabana, 2005, 1997b]. Common to them all is that the stiffness description of the body is simple and easily obtainable. E.g. for beam like bodies structural mechanics can be applied while more dense and arbitrary looking bodies can be modeled using a general purpose finite element solver. The inertia description, on the other hand, becomes cumbersome and highly non-linear due to the fact deformations are described with respect to a local reference frame that undergoes large rotations. Another limiting factor is that small strains and linear material behavior is assumed. This means that large and non-linear deformation problems is not directly treatable using the Floating Frame of Reference Formulation.

To further enhance the modeling of bodies that undergo both large overall motion and large deformation, the Absolute Nodal Coordinate Formulation (ANCF) was introduced by Shabana [1996]. Shortly after the first journal papers were published [Shabana, 1997a; Shabana and Christensen, 1997]. The ANCF is a non-incremental finite element formulation capable of describing large overall displacements in a straight forward manner. This is accomplished by applying two concepts that when combined are unique for the ANCF:

- Nodal positions are described using position vectors expressed in the global inertial reference frame.
- Nodal orientations are described using slope vectors of the position field.

Using these concepts, a set of element generalized coordinates consisting of nodal positions and slope vectors is chosen. The position field spanned by the nodes is described by interpolation of the nodal positions and slopes by appropriate interpolation functions. Throughout this report, a slope vector denotes the first order gradient of a position vector field. There are several benefits associated to the use of global positions and slope vectors when describing the element kinematics. The most significant one is the use of slope vectors to define nodal orientations. Since a vector can be oriented arbitrarily, no assumptions are made regarding nodal rotations. This means that ANCF elements can exhibit arbitrary large rotations and hereby relaxing the assumption of small nodal rotations. Furthermore, these slope vectors does not have to be perpendicular to each other or to be unit vectors. This means that the slope vectors can be used to describe cross section deformation and rotation, which increases the modeling fidelity [Sopanen and Mikkola, 2003]. Furthermore, the use of global parameters as generalized coordinates leads to a constant mass matrix

and zero centrifugal and Coriolis forces [Shabana and Yakoub, 2001]. This simple inertia description makes ANCF attractive for implementation in the multibody dynamics framework.

The use of global position and slope vectors as generalized coordinates is not without problems. Because the element kinematics is based on positions, element strains must be calculated in a way such that rigid body motion produce zero strain. Furthermore, elements that have initial curvature or are skew in their reference configuration must be modeled with care, to remove any initial strain energy that could influence simulation results. In general, the stiffness description of ANCF elements is quite cumbersome and several different techniques have been applied to derive the internal elastic forces. Techniques, ranging from simple structural mechanics [Gerstmayr and Shabana, 2005] to advanced beam theories [Nachbagauer et al., 2011] or full continuum mechanics [Sopanen and Mikkola, 2003].

So far several types of different ANCF based finite elements of both beam and shell types have been proposed. The most extensive research have been done within beam type elements. Here several different combinations of generalized coordinates and stiffness descriptions have been investigated. These extensive studies have led to reports and treatment of severe problems with different locking mechanisms [García-Vallejo et al., 2007]. Because of the intensive work of enhancing the beam ANCF elements, ANCF beam elements have been applied successfully in real life problems such as tire modeling [Sugiyama and Suda, 2009], leaf spring modeling [Omar et al., 2004], catenary systems [Seo et al., 2006; Lee and Park, 2013] and underground cable installation [Yang et al., 2013].

Despite the numerous studies within beam elements, ANCF plate and shell elements seems to be lacking the same interest. To this date, only a few different ANCF shell elements can be found in the literature. Those are thick fully parameterized rectangular elements [Shabana and Christensen, 1997; Mikkola and Shabana, 2003; Matikainen and Mikkola, 2005], thin rectangular elements [Dmitrochenko and Pogorelov, 2003; Dufva and Shabana, 2005] and thin triangular elements [Dmitrochenko and Mikkola, 2008]. General to all the shell elements found in the literature, is that they all only have corner nodes, hence 3 and 4 nodes for triangular and quadrilateral elements, respectively. The different shell element formulations are briefly summarized below.

The fully parametrized thick rectangular element accommodates nodal positions and three slope vectors per node as nodal degrees of freedom. This leads to a total of 48 degrees of freedom (d.o.f.) per element in the three dimensional case. The stiffness description has been based both on the Kirchhoff theory [Shabana and Christensen, 1997] and a full continuum mechanics approach [Mikkola and Shabana, 2003]. The use of the full continuum based stiffness description in its pure form is unfavorable, because it leads to both thickness, curvature and shear locking. This leads to an overly stiff representation. The curvature and shear can be treated by applying linear interpolation of the shear angles [Matikainen and Mikkola, 2005], while thickness locking seems to be unaddressed in current studies.

Two different thin rectangular shell formulations are currently available in the literature. The first was introduced by Dmitrochenko and Pogorelov [2003]. The element in their study uses nodal positions, two slope vectors and one second order gradient vector as nodal generalized coordinates. This leads to 48 d.o.f. per element. The two first order gradient vectors are used to describe in-plane deformation while the second order gradient vectors are associated to the curvature of the element. In their study, several models to calculate the internal elastic forces are presented and validated with exact models with good agreement. Dmitrochenko and Pogorelov [2003] also mention the possibility to construct a simplified element with only 36 d.o.f. This should be done by omitting the second

order slope vectors from the generalized coordinates. Such an element is described and implemented by Dufva and Shabana [2005]. The stiffness description in their study is based purely on the Kirchhoff shell theory, and numerical results are compared to results obtained using the fully parameterized element by Mikkola and Shabana [2003]. The comparison shows that the element by Dufva and Shabana [2005] shows significantly better convergence and faster computational speed.

The paper by Dmitrochenko and Mikkola [2008] introduces two simple triangular shell elements. Most simple is a 18 d.o.f. element based on the conventional triangular finite element by Morley [1971]. This element uses the nodal positions and slope vectors on the midpoint of each element side as nodal degrees of freedom. The second triangular element is based on the conventional triangular finite element originally introduced by Specht [1988]. This element accommodates both nodal displacements and two slope vectors as nodal degrees of freedom. This leads to a total of 27 d.o.f. for the element. For both triangular elements, the interpolation shape functions are derived in terms of triangular coordinates [Zienkiewicz and Taylor, 2000; Specht, 1988] and the stiffness descriptions are based on the Kirchhoff shell theory. The difference in choice of type and number of generalized coordinates, leads to significant differences in the kinematic description of the two elements. The 27 d.o.f. element will ensure a continuous displacement field along element sides, where as the 18 d.o.f. element lacks this property. The lack of displacement continuity can lead to gaps between elements which could affect simulation results. This is demonstrated in the paper by Dmitrochenko and Mikkola [2008]. As an improvement to the 18 d.o.f. triangular element, Dmitrochenko and Mikkola suggests that constraint equations can be used to enforce displacement continuity at element mid-sides, which improves results significantly for the 18 d.o.f. element. These constraints are imposed by equality constraints that enforces the midpoints on adjacent elements to be coincident at any time.

When reviewing the number of publications and the extent of the investigations done regarding ANCF shell elements, it is evident that these are in need of further attention. It should be investigated whether the kinematic description from the conventional finite element method can be reused in the large displacement ANCF elements. Furthermore, to this day, no thorough comparison have been made between any of the above mentioned ANCF shell formulations and e.g. conventional large displacement finite element solutions or analytical models. In general, the validation of the ANCF shell formulations has been based purely on simple and academic models, e.g. simply supported rectangular plates under uniform and symmetric loading. Since all the ANCF models, used in the validation studies, are based on uniform and pure rectangular mesh, validation should be expanded to include arbitrary and distorted mesh.

The remainder of this report is devoted to review and discussion of some of the current ANCF shell formulations. Emphasis is on thin rectangular ANCF shell elements, since they apply to a broad range of engineering structures such as car body structures and wind turbine blades. First, a thorough review of the kinematic descriptions used in the current thin rectangular ANCF shells is given. This introduction will also contain a derivation of the equations of motion. Subsequently, a novel ANCF shell finite element with dynamic mesh properties is reviewed. This element is characterized by being able to change its size during transient simulation. The following chapter contains a preliminary study of the kinematics and numerical performance of thin rectangular ANCF shell elements when used in a curved and distorted mesh. At the end, the content of this report is summed up in a conclusion, and the outlines of the future work is presented in a following chapter.

Chapter 2

# Absolute Nodal Coordinate Formulation

This chapter is devoted to give a review of thin rectangular ANCF shell elements. Initially, a general introduction to ANCF shell elements are given. This is followed by a review of the thin ANCF shell element formulations currently available in the literature. That being the 48 d.o.f. and 36 d.o.f. elements presented by Dmitrochenko and Pogorelov [2003] and the 36 d.o.f. element by Dufva and Shabana [2005]. Since the only difference between these 3 elements is the kinematic description, this will be reviewed for each of them in separate subsections. At the end of the chapter the equations of motion will be derived. This derivation is general and applies to all the elements mentioned in this chapter.

## 2.1 Kinematics of ANCF shell elements

A general three dimensional ANCF shell finite element in an arbitrary configuration is shown in Figure 2.1. The element is spanned by 4 nodes located at each corner of the element midplane. The nodes are numbered 1 through 4 in a counterclockwise order and a local element coordinate system $xyz$ is located at node 1. The position of an arbitrary

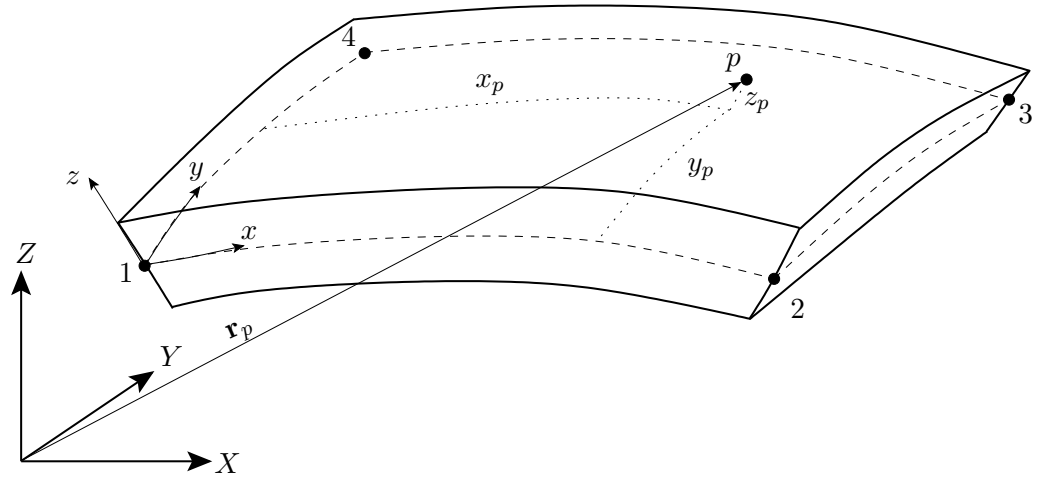


Figure 2.1: An ANCF shell element shown with its local element coordinate system. The dashed lines symbolizes the element midplane.

point $p$ located in the element volume is described by the position vector $\mathbf{r}_p$ expressed with respect to the global inertial reference frame $XYZ$. The position of an arbitrary point in the element volume can be expressed by interpolation of the nodal generalized coordinates

using a set of interpolation shape functions.

$$\mathbf{r} = \mathbf{N}\mathbf{q} \tag{2.1}$$

where $\mathbf{N}$ is a matrix containing the interpolation shape functions and $\mathbf{q}$ is the vector of element generalized coordinates. The vector of generalized coordinates contains information regarding the element configuration, such as the nodal positions and orientations. The generalized coordinates are all expressed with respect to the global reference frame. The interpolation shape functions $\mathbf{N}$ are functions of the local element coordinates $x$, $y$, and $z$ and can be derived using different approaches depending on the element application and choice of generalized coordinates. The shape functions are, in the general case, always constant in time, while the generalized coordinates are changing over time.

Using the relationship in equation (2.1), the position vector $\mathbf{r}_p$ is obtained by evaluating the shape function matrix at the local coordinates $(x_p, y_p, z_p)$ and multiplying it by the vector of nodal coordinates at the time instance $t_p$ corresponding to the element configuration at Figure 2.1:

$$\mathbf{r}_p = \mathbf{N}\left(x_p, y_p, z_p\right)\mathbf{q}\left(t_p\right) \tag{2.2}$$

The simple kinematic relation between the nodal coordinates and an arbitrary point in the element volume makes it straight forward to calculate the velocity $\dot{\mathbf{r}}$ and acceleration $\ddot{\mathbf{r}}$ of an arbitrary point. This is done simply by taking the 1st and 2nd order time derivatives of equation (2.1)

$$\begin{aligned}\dot{\mathbf{r}} &= \mathbf{N}\dot{\mathbf{q}} \\ \ddot{\mathbf{r}} &= \mathbf{N}\ddot{\mathbf{q}}\end{aligned} \tag{2.3}$$

This simplifies the task of deriving equations of motion for a ANCF element significantly, which will become clear in section 2.2.

When determining the number and type of slope vectors that should be used as nodal d.o.f., the element application should be kept in mind. The choice of slope vectors are referred to as the level of element parametrization. If a thick plate structure is considered,

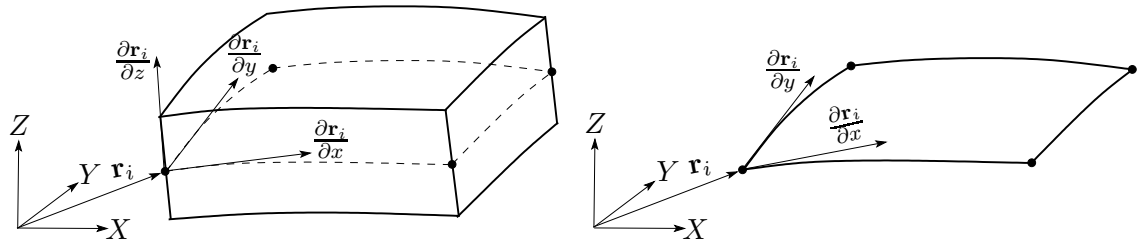


(a) Thick ANCF shell element (b) Thin ANCF shell element

Figure 2.2: Two different parametrization of ANCF shell elements shown with position and slope vectors.

an element parametrization as shown on Figure 2.2a would be a good choice. This element accommodates the nodal positions $\mathbf{r}_i$ and the 3 slope vectors $\frac{\partial \mathbf{r}_i}{\partial x}$, $\frac{\partial \mathbf{r}_i}{\partial y}$ and $\frac{\partial \mathbf{r}_i}{\partial z}$ as nodal degrees of freedom. This parametrization is often referred to as a full parametrization and leads to an element with 48 d.o.f. The in-plane slope vectors $\frac{\partial \mathbf{r}_i}{\partial x}$ and $\frac{\partial \mathbf{r}_i}{\partial y}$ defines the slope of the midplane at the nodes, while the transverse slope vector $\frac{\partial \mathbf{r}_i}{\partial z}$ describes cross

section orientation and deformation. Due to the transverse slope vector $\frac{\partial \mathbf{r}_i}{\partial z}$, this element can describe both transverse normal strain and shear deformation. This is beneficial when analyzing shell structures that have a substantial thickness.

When analyzing thin shell structures, the structure can be modeled using elements where the transverse slope vector $\frac{\partial \mathbf{r}_i}{\partial z}$ is omitted as seen in Figure 2.2b. This leads to a set of element generalized coordinates composed of the nodal positions $\mathbf{r}_i$ and the two in-plane first order gradient vectors $\frac{\partial \mathbf{r}_i}{\partial x}$ and $\frac{\partial \mathbf{r}_i}{\partial y}$. Because the element generalized coordinates lacks a gradient vector, such an element is called as gradient deficient or under parametrized. Since the element is missing coordinates to describe thickness and cross section deformation, the element is modeled entirely by its midplane. This means that the element basically is a membrane.

The gradient deficient shell element is found to have a superior computational performance compared to the fully parametrized elements when analyzing structures with small thickness [Dufva and Shabana, 2005]. Here, a significantly better performance is noted when comparing both convergence and simulation time for models with small element thicknesses. Based on this discovery, emphasis in the remainder of this report is on elements where the transverse slope vectors are omitted from the element generalized coordinates. The kinematics of such three elements are reviewed in the following subsections.

### 2.1.1 Kinematics of the 48 d.o.f. element by Dmitrochenko & Pogorelov

Traditional plate finite elements usually accommodates one nodal displacement and two out-of-plane rotational degrees of freedom. An example of such an element, is the Kirchhoff element family [Cook et al., 2002]. For improved modeling of the element displacement field, an additional degree of freedom based on a 2nd order derivative can be added [Zienkiewicz and Taylor, 2000] leading to 16 d.o.f. Using this improved element kinematics as a base, Dmitrochenko and Pogorelov [2003] formulated a 48 d.o.f. ANCF shell element. The element is shown in its reference configuration in Figure 2.3. The element is assumed to have length $L$, width $W$ and constant thickness $t$. The element uses the nodal positions,

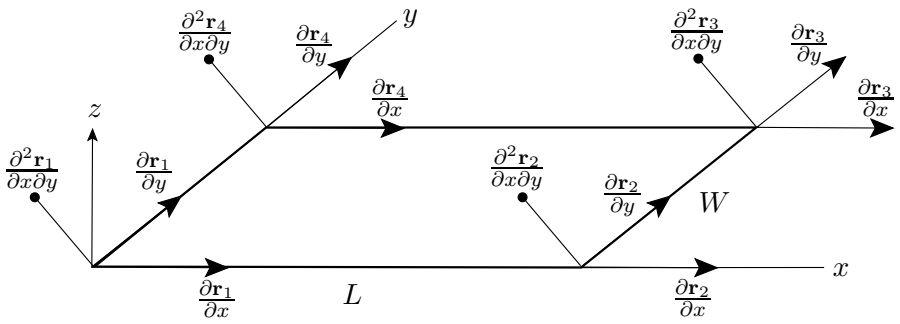


Figure 2.3: A 48 d.o.f. ANCF shell element shown in its undeformed reference configuration with the 1st and 2nd order slope vectors that are used as generalized coordinates.

the two in-plane slope vectors, and a 2nd order slope vector as generalized coordinates:

$$\mathbf{q} = \left[ \mathbf{r}_1^T \left(\frac{\partial \mathbf{r}_1}{\partial x}\right)^T \left(\frac{\partial \mathbf{r}_1}{\partial y}\right)^T \left(\frac{\partial^2 \mathbf{r}_1}{\partial x \partial y}\right)^T \quad \dots \quad \mathbf{r}_4^T \left(\frac{\partial \mathbf{r}_4}{\partial x}\right)^T \left(\frac{\partial \mathbf{r}_4}{\partial y}\right)^T \left(\frac{\partial^2 \mathbf{r}_4}{\partial x \partial y}\right)^T \right]^T \tag{2.4}$$

The interpolation shape functions for the shell element are derived using products of Hermite polynomials [Zienkiewicz and Taylor, 2000]. This approach is sometimes referred to

as the crossed beam technique. The element shape functions are derived in full details in Appendix A. The Hermite polynomials have a certain characteristic, namely that a Hermite polynomial of order $2n+1$ leads to $C^n$ continuity between adjacent elements. Based on the chosen generalized coordinates, a 3rd order Hermitian interpolation is applied. This leads to $C^1$ continuous shape functions. In the literature, $C^1$ continuity is mentioned as a theoretically indispensably requirement when the element stiffness properties are calculated based on the element curvature [Zienkiewicz and Taylor, 2000; Gerstmayr et al., 2012]. This is due to the fact that the curvature of the overall displacement field will be infinite at the boundary between 2 adjacent elements if there is a discontinuity in slope. The necessity of $C^1$ continuous shape functions will be discussed in Chapter 4.

### 2.1.2 Kinematics of the 36 d.o.f. element by Dmitrochenko & Pogorelov

As an alternative to the 48 d.o.f. element, Dmitrochenko and Pogorelov suggests a reduced order element. This is done by removing the 2nd order gradient vectors from the generalized coordinates. See Figure 2.4. Hereby the number of d.o.f. reduces to 36 given by:

$$\mathbf{q} = \left[ \mathbf{r}_1^T \left(\frac{\partial \mathbf{r}_1}{\partial x}\right)^T \left(\frac{\partial \mathbf{r}_1}{\partial y}\right)^T \quad \dots \quad \mathbf{r}_4^T \left(\frac{\partial \mathbf{r}_4}{\partial x}\right)^T \left(\frac{\partial \mathbf{r}_4}{\partial y}\right)^T \right]^T \tag{2.5}$$

Using this coordinate set, the element coordinates correspond to those used in the normal Kirchhoff plate bending elements known from the traditional finite element method [Cook et al., 2002]. The shape functions are obtained directly using the crossed beam technique as in the full 48 d.o.f. element, and omitting shape functions associated to the $\frac{\partial^2 \mathbf{r}}{\partial x \partial y}$. This results in a shape function matrix containing only 12 unique functions.

The exclusion of the 2nd order gradients from the generalized coordinates have a few advantages. First and foremost, the number of degrees of freedom reduces from 48 to 36. Furthermore, the $\frac{\partial^2 \mathbf{r}}{\partial x \partial y}$ gradient vector have no clear geometrical meaning, which makes it difficult to interpret. In Chapter 4, results obtained using this reduced order element are compared to results using the 48 d.o.f. ANCF element.

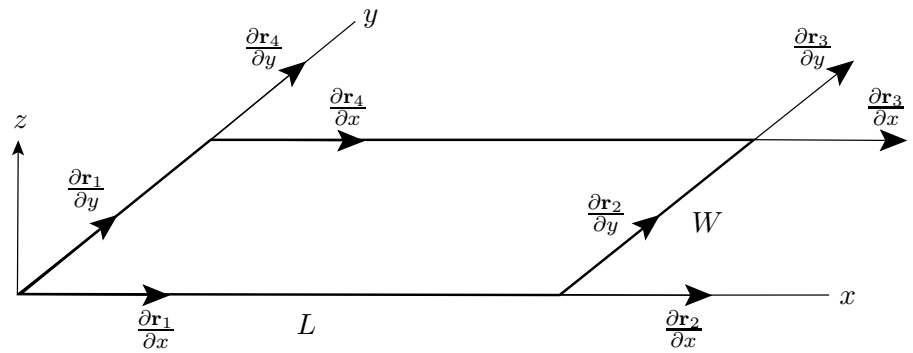


Figure 2.4: A 36 d.o.f. ANCF shell element shown with the slope vectors used as generalized coordinates.

### 2.1.3 Kinematics of the 36 d.o.f. element by Dufva & Shabana

The final element which will be reviewed here, is the element by Dufva and Shabana [2005]. This uses the same 36 d.o.f. as suggested in the paper by Dmitrochenko and Pogorelov

[2003]. See Figure 2.4 and equation (2.5). The derivation of the element shape functions on the other hand is different. In their study, it is assumed that the position field can be described using the following incomplete quartic polynomial:

$$\mathbf{r} = \begin{bmatrix} a_1 + a_2x + a_3y + a_4x^2 + a_5xy + a_6y^2 + a_7x^3 + \\ b_1 + b_2x + b_3y + b_4x^2 + b_5xy + b_6y^2 + b_7x^3 + \\ c_1 + c_2x + c_3y + c_4x^2 + c_5xy + c_6y^2 + c_7x^3 + \\ \qquad a_8x^2y + a_9xy^2 + a_{10}y^3 + a_{11}x^3y + a_{12}xy^3 \\ \qquad b_8x^2y + b_9xy^2 + b_{10}y^3 + b_{11}b^3y + b_{12}xy^3 \\ \qquad c_8x^2y + c_9xy^2 + c_{10}y^3 + c_{11}c^3y + c_{12}xy^3 \end{bmatrix} \tag{2.6}$$

Here, $a_i$, $b_i$ and $c_i$ are the polynomial coefficients which will vary in time in the case of transient simulations. Note that the position field does not contain any terms that describes variations in the transverse direction $z$. A set of interpolation shape functions $\mathbf{N}$ that depends only on the local element coordinates $x$ and $y$ and the element length $L$ and width $W$ can be obtained using matrix operations. In this way, the position field can be expressed in the more convenient way shown in equation (2.1). The derivation of the shape function using this approach are shown in full details in Appendix B. It can be shown that the shape functions obtained using this approach ensures only $C^0$ continuity. This could lead to differences in numerical solutions when compared to the $C^1$ continuous formulation used in the element by Dmitrochenko and Pogorelov [2003]. It will be investigated in Chapter 4 whether this is the case.

## 2.2 Equations of motion

The equations of motion for an ANCF element can be calculated in several manners, e.g. using the D'Alembert-Lagrange equations or Hamilton's principle [Shabana, 2005]. Another way is to calculate the virtual work $\delta W$ for a system in dynamic equilibrium:

$$\delta W = \delta W_f - \delta W_i - \delta W_e = 0 \tag{2.7}$$

Here $\delta W_f$, $\delta W_i$, and $\delta W_e$ denote the virtual work done by external, inertial and internal elastic forces, respectively. The virtual work done by the external and inertial forces can be calculated as follows.

$$\begin{aligned} \delta W_f &= \int_V \delta \mathbf{r}^T \mathbf{F} \mathrm{d}V \\ \delta W_i &= \int_V \delta \mathbf{r}^T \ddot{\mathbf{r}} \rho \mathrm{d}V \end{aligned} \tag{2.8}$$

where $\mathbf{F}$ is the total externally applied force vector consisting of external and constraint forces, and $\rho$ is the material density. The virtual displacement $\delta\mathbf{r}$ can be expressed in terms of the generalized coordinates and the shape functions as:

$$\delta \mathbf{r} = \mathbf{N} \delta \mathbf{q} \tag{2.9}$$

The virtual work done by the internal elastic forces for a thin ANCF shell element can be calculated using the Kirchhoff plate theory [Timoshenko and Woinowsky-Krieger, 1959]. Here, the elastic energy is segregated in to two parts. One part consists of the energy arising due to membrane stretch and shear while the other part accounts for the energy

arising due to bending and twisting of the midplane. The virtual work of elastic forces is expressed as:

$$\delta W_e = \int_V \delta\boldsymbol{\epsilon}^T \mathbf{E}\ \boldsymbol{\epsilon} \mathrm{d}V + \int_V \delta\boldsymbol{\kappa}^T \mathbf{E}\ \boldsymbol{\kappa} \mathrm{d}V, \tag{2.10}$$

where $\boldsymbol{\epsilon}$ is a vector containing the in-plane normal and shear strains, $\boldsymbol{\kappa}$ is a vector containing midplane curvatures and $\mathbf{E}$ is the constitutive matrix. The in-plane strains for an initially straight and rectangular element with the local element coordinate system aligned with the global inertial reference frame is calculated using the general non-linear Green-Lagrange strain tensor:

$$\begin{aligned} &\boldsymbol{\epsilon} = [\epsilon_{xx} \quad \epsilon_{yy} \quad 2\epsilon_{xy}]^T \\ &\epsilon_{xx} = \frac{\left(\frac{\partial \mathbf{r}}{\partial x}\right)^T \left(\frac{\partial \mathbf{r}}{\partial x}\right) - 1}{2}, \quad \epsilon_{yy} = \frac{\left(\frac{\partial \mathbf{r}}{\partial y}\right)^T \left(\frac{\partial \mathbf{r}}{\partial y}\right) - 1}{2}, \quad \epsilon_{xy} = \frac{\left(\frac{\partial \mathbf{r}}{\partial x}\right)^T \left(\frac{\partial \mathbf{r}}{\partial y}\right) - 1}{2} \end{aligned} \tag{2.11}$$

and the curvature is calculated as [Dufva and Shabana, 2005]:

$$\begin{aligned} &\boldsymbol{\kappa} = z\,[\kappa_{xx} \quad \kappa_{yy} \quad 2\kappa_{xy}]^T \\ &\kappa_{xx} = \frac{\left(\frac{\partial^2 \mathbf{r}}{\partial x^2}\right)^T \mathbf{n}}{||\mathbf{n}||^3}, \quad \kappa_{yy} = \frac{\left(\frac{\partial^2 \mathbf{r}}{\partial y^2}\right)^T \mathbf{n}}{||\mathbf{n}||^3}, \quad \kappa_{xy} = \frac{\left(\frac{\partial^2 \mathbf{r}}{\partial x \partial y}\right)^T \mathbf{n}}{||\mathbf{n}||^3} \end{aligned} \tag{2.12}$$

The mid-surface normal vector $\mathbf{n}$ is defined as $\mathbf{n} = \frac{\partial \mathbf{r}}{\partial x} \times \frac{\partial \mathbf{r}}{\partial y}$. Note that the vector $\boldsymbol{\kappa}$ is multiplied by a local transverse coordinate $z$ ranging $-t/2 \leq z \leq t/2$. Hereby it is assumed that the bending strains vary linearly over the shell cross section from a maximum tension at $z = -t/2$ to maximum compression at $z = t/2$ when subjected to a positive bending moment.

The strains and curvatures are functions of the generalized coordinates. This means the virtual strain $\delta\boldsymbol{\epsilon}$ and virtual curvature $\delta\boldsymbol{\kappa}$ can be expressed as a functions of the generalized coordinates by applying the chain rule of differentiation as

$$\begin{aligned} \delta\boldsymbol{\epsilon} &= \frac{\partial \boldsymbol{\epsilon}}{\partial \mathbf{q}} \delta\mathbf{q} \\ \delta\boldsymbol{\kappa} &= \frac{\partial \boldsymbol{\kappa}}{\partial \mathbf{q}} \delta\mathbf{q} \end{aligned} \tag{2.13}$$

When combining equations (2.3) and (2.7) - (2.13), the total virtual work for an ANCF element can be expressed as:

$$\begin{aligned} \delta\mathbf{q}^T \Bigg( \int_V \mathbf{N}^T \mathbf{F}\ \mathrm{d}V - \int_V \rho \mathbf{N}^T \mathbf{N}\ \mathrm{d}V \ddot{\mathbf{q}} - \int_V \left(\frac{\partial \boldsymbol{\epsilon}}{\partial \mathbf{q}}\right)^T \mathbf{E}\ \boldsymbol{\epsilon}\ \mathrm{d}V - \\ \int_V \left(\frac{\partial \boldsymbol{\kappa}}{\partial \mathbf{q}}\right)^T \mathbf{E}\ \boldsymbol{\kappa} \mathrm{d}V \Bigg) = 0 \end{aligned} \tag{2.14}$$

This equation must hold true for any virtual displacement which leads to the equation of motion that takes this simple form:

$$\mathbf{M}\ddot{\mathbf{q}} = \mathbf{Q}_f - \mathbf{Q}_e \tag{2.15}$$

where

$$\begin{aligned}
\mathbf{M} &= \rho t \int_0^L \int_0^W \mathbf{N}^T \mathbf{N} \, \mathrm{d}y\mathrm{d}x \\
\mathbf{Q}_f &= t \int_0^L \int_0^W \mathbf{N}^T \mathbf{F} \, \mathrm{d}y\mathrm{d}x \\
\mathbf{Q}_e &= t \int_0^L \int_0^W \left( \frac{\partial \boldsymbol{\epsilon}}{\partial \mathbf{q}} \right)^T \mathbf{E} \, \boldsymbol{\epsilon} \, \mathrm{d}y\mathrm{d}x + \int_0^L \int_0^W \int_{-t/2}^{t/2} \left( \frac{\partial \boldsymbol{\kappa}}{\partial \mathbf{q}} \right)^T \mathbf{E} \, \boldsymbol{\kappa} \, \mathrm{d}z\mathrm{d}y\mathrm{d}x
\end{aligned} \tag{2.16}$$

Here; $\mathbf{M}$ is the mass matrix, $\mathbf{Q}_f$ is the vector of external forces, and $\mathbf{Q}_e$ is the vector of elastic forces. Note that the integration limits have been changed because the majority of the expressions are without thickness dependent terms. Therefore, the integral over the thickness can be substituted by multiplying the remainder with the constant element thickness. The only exception is the part of the elastic force vector that is a function of the element curvature. Here, the integral in the transverse direction $z$ is retained, due to the thickness varying bending strains.

The derivation of the equations of motion have clarified some of the advantages and drawbacks associated to the ANCF. First and foremost, the constant mass matrix and the absence of centrifugal and Coriolis forces is highly notable. This is a consequence of using generalized coordinates expressed in a global reference frame. Because the mass matrix remains constant over time, it can be evaluated in a pre-processing step before the actual simulation forward in time is performed. Furthermore, the integral in the expression for the mass matrix can, in general, be solved analytically. The same goes for the expression of the external forces. This ensures fast numerical evaluation. The simple expressions for the mass matrix and external forces, together with the simple kinematic description, are the key benefits that makes the ANCF attractive for implementation in the multibody dynamics framework.

As mentioned in the introduction, the ANCF is not without difficulties. These difficulties are mainly tied to the vector of elastic forces. In general, the elastic forces are highly non-linear functions of the generalized coordinates. Even when the elastic forces are based on simple expressions from the structural mechanics. In this case where the Kirchhoff plate theory is applied, it is in particular the expressions for the element curvature that are highly non-linear. See equation 2.12. Because of the non-linearity of the elastic forces, there exist no closed form solution to the integrals. See equation 2.16. Instead, the vector of elastic forces must be calculated using numerical integration, e.g. Gaussian quadrature. This takes a significant amount of computational power since the integrand it self is extensive, and often a large number of sampling points is needed.

Chapter 3

# ALE-ANCF based shell element

This chapter contains a short review of the shell element introduced by Hyldahl *et al.* [Hyldahl et al., 2013]. In this paper a novel shell finite element based on the combined Arbitrary Lagrange-Euler and Absolute Nodal Coordinate Formulations (ALE-ANCF). This element is distinguished by applying extra nodal degrees of freedom to describe the relative nodal positions in the mesh. This allows the nodes to travel in the modeled specimen, making the element particular suited for modeling sliding joints and traveling forces.

## 3.1 Kinematics of ALE-ANCF based shell elements

The combination of the Arbitrary Lagrange-Euler and the Absolute Nodal Coordinate Formulation was introduced to analyze large displacements in very elastic specimens with internal mass flow and sliding joints [Hong et al., 2011; Hong and Ren, 2011]. In these studies focus is on specimens that can be treated as one-dimensional. This leads to a structural description based on well-known beam theory. The innovation associated to the study is the kinematic description. Here, the authors are inspired by the mobile element kinematics known from the Arbitrary Lagrange-Euler (ALE) description [Donea et al., 2004]. In the ALE description, the nodal positions are not fixed either to the modeled specimen or to the global reference frame. In stead, the nodes are allowed to move arbitrarily, which can be of great advantage in cases where either the domain or the specimen undergo large deformation. Therefore the ALE mesh description is widely used e.g. in Computational Fluid Dynamics (CFD) or non-linear solid mechanics. A good example were the ALE description is advantageous, is in the simulation of forming processes of metals. Here, significant re-meshing can be avoided when applying the ALE method [Schreurs et al., 1986].

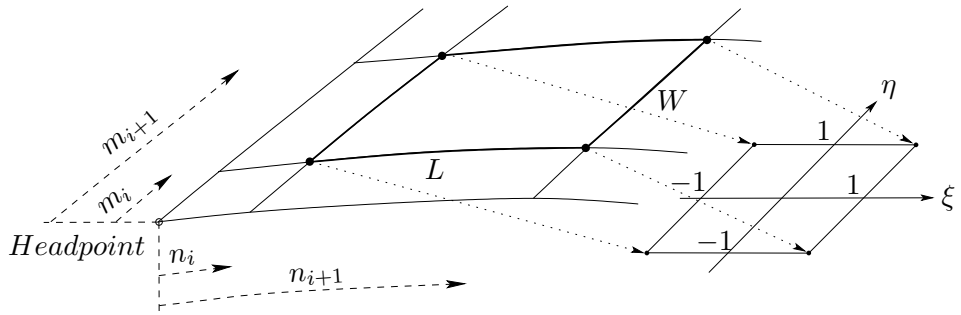


Figure 3.1: Plate element in two-dimensional mesh mapped in to isoparametric coordinates

The idea of the moving nodes is transfered to the ANCF to formulate the kinematics of an ANCF shell element with non-stationary nodes. An additional set of generalized

coordinates $n_i$ and $m_i$ that describes the nodal position in the modeled specimen is introduced. See Figure 3.1. The position of the nodes are measured with respect to a fixed reference point called as the head point. Often the head point is located at a corner of the modeled specimen. Combining the extra set of local material coordinates with the general ANCF coordinates, see equation (2.5), results in an expression for the total vector element generalized coordinates.

$$\begin{aligned}
\mathbf{q}_e &= \left[\mathbf{r}_1^T \left(\frac{\partial \mathbf{r}_1}{\partial x}\right)^T \left(\frac{\partial \mathbf{r}_1}{\partial y}\right)^T \quad \dots \quad \mathbf{r}_4^T \left(\frac{\partial \mathbf{r}_4}{\partial x}\right)^T \left(\frac{\partial \mathbf{r}_4}{\partial y}\right)^T\right]^T \\
\mathbf{q}_l &= \begin{bmatrix} n_1 & m_1 & n_2 & m_2 \end{bmatrix}^T \\
\mathbf{q} &= \begin{bmatrix} \mathbf{q}_e^T & \mathbf{q}_l^T \end{bmatrix}^T
\end{aligned} \tag{3.1}$$

where $\mathbf{q}_e$ is the vector of ANCF coordinates, $\mathbf{q}_l$ are the local material coordinates, and $\mathbf{q}$ is the full vector of generalized coordinates. By the introduction of the coordinates $n_i$ and $m_i$, the elements are allowed to change their sizes dynamically over time. This means that the isoparametric mapping of each element becomes unique and time dependent. The varying isoparametric mapping is accounted for by expressing the isoparametric mapping parameters $\xi$ and $\eta$ in terms of the local material coordinates $n_i$ and $m_i$.

$$\begin{aligned}
\xi &= \frac{2n - n_1 - n_2}{n_2 - n_1} \\
\eta &= \frac{2m - m_1 - m_2}{m_2 - m_1}
\end{aligned} \tag{3.2}$$

Furthermore, the element side lengths can be expressed in terms of $n_i$ and $m_i$.

$$\begin{aligned}
L &= n_2 - n_1 \\
W &= m_2 - m_1
\end{aligned} \tag{3.3}$$

The position vector of an arbitrary point on an element $\mathbf{r}$ is obtained in the normal manner by interpolation of the nodal position and slope vectors.

$$\mathbf{r} = \mathbf{N}_e \mathbf{q}_e \tag{3.4}$$

where $\mathbf{N}_e$ is the $3\times36$ interpolation shape function matrix and $\mathbf{q}_e$ is the vector of generalized ANCF nodal coordinates. The shape functions can be derived using either the crossed beam technique or based on an incomplete quartic polynomial, see equation (2.6). In this study, shape functions based on the crossed beam technique are chosen.

Because of the time varying isoparametric mapping, the shape functions are functions of the local material coordinates $n_i$ and $m_i$. This means that the shape functions are time dependent. Because of the shape function time dependency, the chain rule of differen-tiation must be applied when calculating the velocity and acceleration of an arbitrary point.

$$\begin{aligned}
\dot{\mathbf{r}} &= \mathbf{N}_e \dot{\mathbf{q}}_e + \frac{\partial \mathbf{N}_e}{\partial t} \mathbf{q}_e \\
\ddot{\mathbf{r}} &= \mathbf{N}_e \ddot{\mathbf{q}}_e + 2\frac{\partial \mathbf{N}_e}{\partial t} \dot{\mathbf{q}}_e + \frac{\partial^2 \mathbf{N}_e}{\partial t^2} \mathbf{q}_e
\end{aligned} \tag{3.5}$$

It can be shown that by rearranging and collecting terms that the velocity and acceleration vectors can be written in simpler form:

$$\begin{aligned}
\dot{\mathbf{r}} &= \mathbf{N}\dot{\mathbf{q}} \\
\ddot{\mathbf{r}} &= \mathbf{N}\ddot{\mathbf{q}} + \ddot{\mathbf{r}}_p
\end{aligned} \tag{3.6}$$

The quantities $\mathbf{N}$ and $\ddot{\mathbf{r}}_p$ take a cumbersome form, and especially $\ddot{\mathbf{r}}_p$ is a highly non-linear function of both the nodal coordinates and the nodal velocities. $\mathbf{N}$ and $\ddot{\mathbf{r}}_p$ are given by:

$$\begin{aligned}\mathbf{N} &= [\mathbf{N}_e \;\; \mathbf{N}_q] \\ \mathbf{N}_q &= \left[ \frac{\partial \mathbf{N}_e}{\partial n_1}\mathbf{q}_e \;\; \frac{\partial \mathbf{N}_e}{\partial m_1}\mathbf{q}_e \;\; \frac{\partial \mathbf{N}_e}{\partial n_2}\mathbf{q}_e \;\; \frac{\partial \mathbf{N}_e}{\partial m_2}\mathbf{q}_e \right]\end{aligned} \tag{3.7}$$

and

$$\ddot{\mathbf{r}}_p = 2\mathbf{N}_{qt}\dot{\mathbf{q}}_l + \mathbf{N}_{qq}\dot{\mathbf{q}}_l^2 + 2\mathbf{N}_{tt}\mathbf{q}_e \tag{3.8}$$

where

$$\mathbf{N}_{qt} = \left[ \frac{\partial \mathbf{N}_e}{\partial n_1}\dot{\mathbf{q}}_e \;\; \frac{\partial \mathbf{N}_e}{\partial m_1}\dot{\mathbf{q}}_e \;\; \frac{\partial \mathbf{N}_e}{\partial n_2}\dot{\mathbf{q}}_e \;\; \frac{\partial \mathbf{N}_e}{\partial m_2}\dot{\mathbf{q}}_e \right]$$

$$\mathbf{N}_{qq} = \left[ \frac{\partial^2 \mathbf{N}_e}{\partial n_1^2}\mathbf{q}_e \;\; \frac{\partial^2 \mathbf{N}_e}{\partial m_1^2}\mathbf{q}_e \;\; \frac{\partial^2 \mathbf{N}_e}{\partial n_2^2}\mathbf{q}_e \;\; \frac{\partial^2 \mathbf{N}_e}{\partial m_2^2}\mathbf{q}_e \right] \tag{3.9}$$

$$\begin{aligned}\mathbf{N}_{tt} = {} & \frac{\partial^2 \mathbf{N}_e}{\partial n_1 \partial m_1}\dot{n}_1\dot{m}_1 + \frac{\partial^2 \mathbf{N}_e}{\partial n_1 \partial n_2}\dot{n}_1\dot{n}_2 + \frac{\partial^2 \mathbf{N}_e}{\partial n_1 \partial m_2}\dot{n}_1\dot{m}_2 + \\ & \frac{\partial^2 \mathbf{N}_e}{\partial m_1 \partial n_2}\dot{m}_1\dot{n}_2 + \frac{\partial^2 \mathbf{N}_e}{\partial m_1 \partial m_2}\dot{m}_1\dot{m}_2 + \frac{\partial^2 \mathbf{N}_e}{\partial n_2 \partial m_2}\dot{n}_2\dot{m}_2\end{aligned}$$

## 3.2 Equations of motion

The equations of motion for an ALE-ANCF element is derived as in the traditional ANCF by employing the principle of virtual work, see equation (2.7). In the calculation of the virtual work, the virtual displacement $\delta\mathbf{r}$ is needed. As in the general ANCF, $\delta\mathbf{r}$ can be rewritten in terms of the generalized coordinates, but due to the time varying shape functions the chain rule must be applied. The virtual displacement is expressed as:

$$\delta\mathbf{r} = \mathbf{N}_e\delta\mathbf{q}_e + \delta\mathbf{N}_e\mathbf{q}_e = \mathbf{N}\delta\mathbf{q} \tag{3.10}$$

The virtual work done by the applied and elastic forces are calculated in a straight forward manner as in the general ANCF. See equations (2.8) and (2.10). The virtual work done by the inertia forces $\delta W_i$ takes a more extensive form due to the extra terms in the acceleration vector. See equation (3.6). The virtual work done by the inertia forces is calculated as:

$$\begin{aligned}\delta W_i &= \rho \int_V \delta\mathbf{r}^T \left(\mathbf{N}\ddot{\mathbf{q}} + \ddot{\mathbf{r}}_p\right) \mathrm{d}V \Leftrightarrow \\ \delta W_i &= \delta\mathbf{q}^T \left( \rho \int_V \mathbf{N}^T\mathbf{N}\mathrm{d}V\ddot{\mathbf{q}} + \rho \int_V \mathbf{N}^T\ddot{\mathbf{r}}_p \mathrm{d}V \right)\end{aligned} \tag{3.11}$$

This shows that, in addition to a traditional mass matrix, an additional inertial force vector arises. The equations of motion is assembled by combining equation 3.11 with the expressions for the virtual work done by the external and elastic forces. The constraint

reaction forces are accounted for by using Lagrange multipliers [Haug, 1989]. Hereby, the equations of motion for an ALE-ANCF shell element takes the form:

$$\mathbf{M}\ddot{\mathbf{q}} = \mathbf{Q}_f - \mathbf{Q}_e - \mathbf{Q}_p - \left(\frac{\partial \mathbf{\Phi}}{\partial \mathbf{q}}\right)^T \boldsymbol{\lambda} \tag{3.12}$$

with

$$\begin{aligned}
\mathbf{M} &= \rho t \int_{n_1}^{n_2} \int_{m_1}^{m_2} \mathbf{N}^T \mathbf{N} \, \mathrm{d}m\mathrm{d}n \\
\mathbf{Q}_f &= \int_{n_1}^{n_2} \int_{m_1}^{m_2} \mathbf{N}^T \mathbf{F} \, \mathrm{d}m\mathrm{d}n \\
\mathbf{Q}_e &= t \int_{n_1}^{n_2} \int_{m_1}^{m_2} \left(\frac{\partial \boldsymbol{\epsilon}}{\partial \mathbf{q}}\right)^T \mathbf{E}\, \boldsymbol{\epsilon} \, \mathrm{d}m\mathrm{d}n + \int_{n_1}^{n_2} \int_{m_1}^{m_2} \int_{-t/2}^{t/2} \left(\frac{\partial \boldsymbol{\kappa}}{\partial \mathbf{q}}\right)^T \mathbf{E}\, \boldsymbol{\kappa} \, \mathrm{d}z\mathrm{d}m\mathrm{d}n \\
\mathbf{Q}_p &= \rho t \int_{n_1}^{n_2} \int_{m_1}^{m_2} \mathbf{N}^T \ddot{\mathbf{r}}_p \, \mathrm{d}m\mathrm{d}n
\end{aligned} \tag{3.13}$$

Here; $\mathbf{M}$ is the element mass matrix, $\mathbf{Q}_f$ is the generalized applied force vector, $\mathbf{Q}_e$ is the vector of elastic forces, and $\mathbf{Q}_p$ is an inertia force vector that depends quadratically on velocities. The constraint reaction forces is calculated as the product of the constraint Jacobian $\frac{\partial \mathbf{\Phi}}{\partial \mathbf{q}}$ and the vector of Lagrange multipliers $\boldsymbol{\lambda}$. The inertia force vector $\mathbf{Q}_p$ is unique for the ALE-ANCF and arises because the acceleration, as defined in equation (3.6), is a function of both the generalized coordinates $\mathbf{q}_e$ and generalized velocities $\dot{\mathbf{q}}_e$. The element mass matrix will also vary with time due to shape function time dependency. However, according to equation (3.8) and (3.9), if the local material coordinates $m_i$ and $n_1$ are kept fixed, then $\dot{n}_i = \dot{m}_i = 0$, and the inertial force vector $\mathbf{Q}_p$ will be zero. The mass matrix on the other hand will continue to vary with time, because the 4 last terms in the full shape matrix $\mathbf{N}$ are functions of the nodal coordinates $\mathbf{q}_e$. See equation (3.7). In general, this means the elements in the mass matrix associated with the material coordinates $n_i$ and $m_i$ will retain their time dependency even if the material coordinates are kept fixed. In this way, the ALE-ANCF method differs from the conventional ANCF method, in which the element mass matrix is constant for all element configurations. However, in some special cases it is possible to modify the equations of motion so the ALE-ANCF mass matrix remains constant. For instance, the mass matrix forced to be constant in a case where all local material coordinates are intentionally kept fixed throughout the entire simulation. In these cases, it is possible to leave out the equations used to obtain solutions for the local material coordinates, and the time dependent terms of the mass matrix vanish. Then, the system of equations reduces to a set that are consistent with the conventional ANCF method.

## 3.3 Numerical example

To demonstrate the ALE-ANCF method's ability to move a node progressively during a simulation a simple model has been constructed. The model consists of 4 ALE-ANCF shell elements arranged in a $2 \times 2$ mesh to form a quadratic shell with a side length of 1 m placed in the global $xy$-plane. In the start configuration, the center node is shifted toward one of the plate corners. See Figure 3.2. A constant force acting in the negative $z$-direction acts on the center node, and the node moves diagonally at a constant velocity toward the

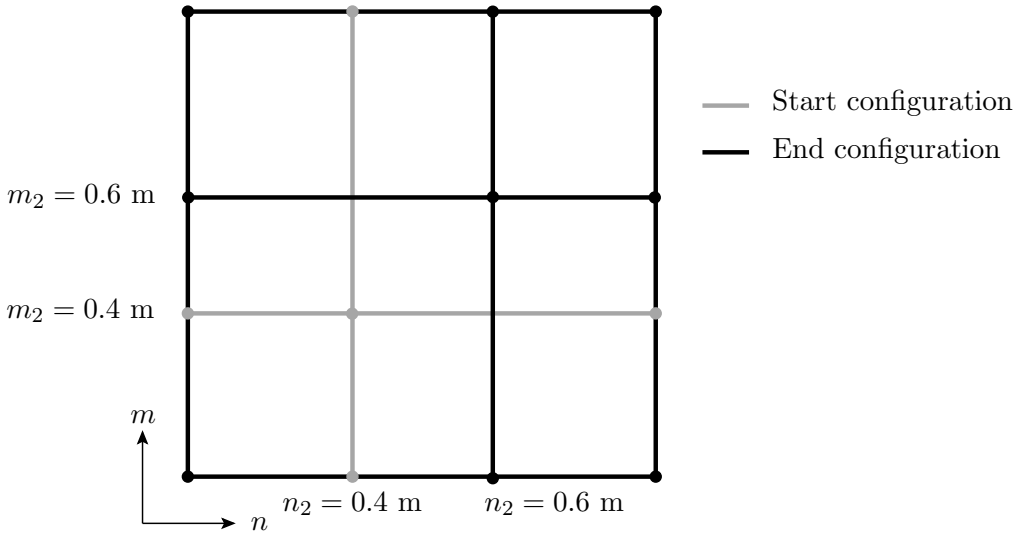


Figure 3.2: ALE-ANCF model with moving node seen from the top

opposite corner during simulation. The translational degrees of freedom for the four corner nodes are fixed to ground and coincident nodes are connected using constraints that ensure both nodal connectivity and slope continuity between adjacent elements. It is important to note that this constraint based assembly technique is essential for making it possible to move the nodes in the mesh during a simulation. The center node is moved from $n, m = 0.4$ m to 0.6 m by imposing a displacement constraint on the $n$ and $m$ coordinates of the 2nd row of nodes, that is $n_2$ and $m_2$. The constraint for the $n_2$-coordinate, $C_n$, can be expressed as follows.

$$C_n = n_2 - v \cdot t, \tag{3.14}$$

where $v$ is the velocity of the moving node. The constraint for the $m_2$-coordinate is expressed in a similar manner by replacing $n_2$ with $m_2$.

The ALE-ANCF model is validated by comparing its center node displacements with displacements obtained from the results of simulations based on conventional ANCF elements based on the 36 d.o.f formulation by Dmitrochenko and Pogorelov [2003]. The comparison displacements are static solutions to analysis where the center node is placed on the diagonal of the plate in a range from $n, m = 0.4$ m to 0.6 m. Static solutions are obtained for 5 intermediate points. For both the ALE-ANCF and conventional ANCF models, the plate material is assumed to be linear elastic and isotropic. The material has a Young's modulus of $1 \times 10^7$ Pa, a Poisson's ratio of 0.3, and a density of 1000 kg/m$^3$. The applied force is $1 \times 10^{-3}$ N. The simulation of the ALE-ANCF model begins from static equilibrium, and the node moves with a velocity of $0.01\frac{\text{m}}{\text{s}}$. The low velocity is chosen to ensure near-static conditions in the ALE-ANCF model for valid comparison with the results from static ANCF solutions. Both sets of results are shown in Figure 3.3. The plot shows that displacements obtained from the continuous simulation based on ALE-ANCF shell elements are comparable with the displacements from static solutions modeled with conventional ANCF elements. Another important physical quantity to validate is the strain level in the plate. To get an overall measure of the strain level in the model, the elastic energy from the dynamic simulation is compared to the elastic energy level resulting from the static ANCF analysis. These elastic energies are shown in Figure 3.4 as a function of

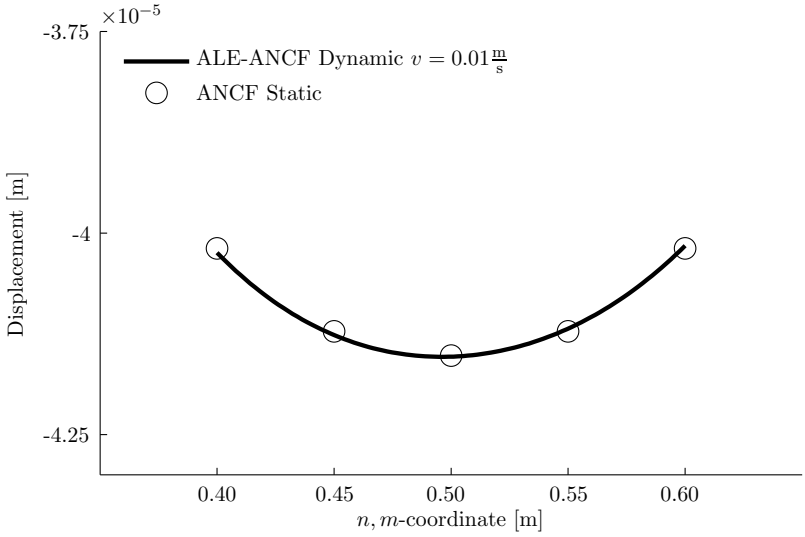


Figure 3.3: Out of plane displacement of the moved node compared with static displacements

the position of the moving node. The elastic energy level from the model based on ALE-ANCF method are consistent with the results obtained with conventional ANCF method. This means that no additional strains are introduced by altering the node position in the mesh.

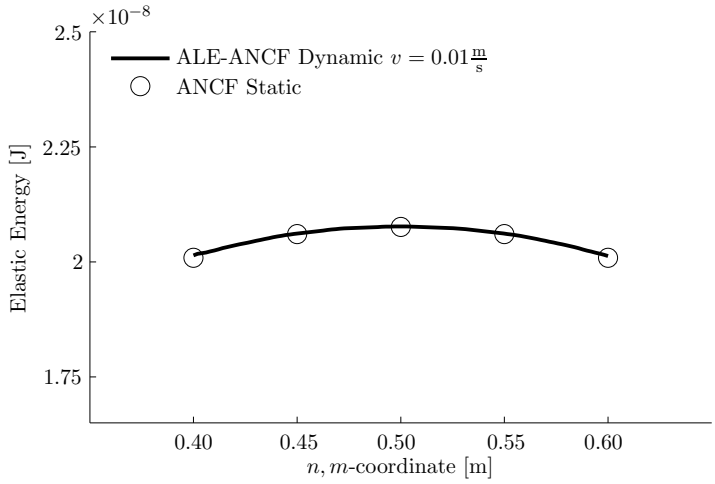


Figure 3.4: The elastic energy in the model compared to energy levels obtained from static analysis

## 3.4 Discussion

This study has shown that it is possible to formulate an ALE-ANCF shell element description that allows interior nodes to move progressively during simulation. The derivation of the ALE-ANCF shell description has revealed one major aspect of the ALE-ANCF description that differs from conventional ANCF element descriptions, namely, the non-constant

inertial description. Beside this difference, the derivation of elastic forces for the ALE-ANCF description follows the same procedure as in the conventional ANCF description.

The proposed ALE-ANCF method has been validated with two numerical studies, where only one is presented here in this report. The first has shown that the proposed ALE-ANCF method is consistent with the conventional ANCF method when ALE-ANCF elements are tied together using algebraic constraints while relative node positions inside the specimen are kept fixed. This property is important if the method is to be applied in cases where movable nodes are only needed during some intervals of a simulation. For further explanation see the original research article [Hyldahl et al., 2013] for the details regarding this first example. The second study presented here demonstrated the ability of the proposed ALE-ANCF method to move a node during simulation. In this simple study, a node was moved across the diagonal of a quadratic plate with a constant velocity. The displacement in the direction normal to the plate and the elastic energy in the model were compared to results obtained using conventional ANCF elements.

The scope of this initial study was to illustrate the methods ability to move a node progressively during transient simulation. This was accomplished using a simple academic example, but more advanced applications are easily imaginable. As mentioned in the introduction of the chapter, the method could be useful when modeling structures with moving boundary conditions such as traveling forces or sliding joints. It is also believed that the ALE-ANCF method could be used as extension to mesh refinement techniques. Using the ALE-ANCF, nodes could travel to areas were large deformation occur to enhance the numerical solution. Another application could be analysis of crack propagation in plate like structures. Taking for instance the model shown in Figure 3.2, a crack could be initiated by omitting the node assembly constraint in one of the nodes on the boundary. This leaves an open gap between two of the elements with a node placed at the end, thus forming a crack. The node at the end of the crack could then be moved to resemble the crack propagating in the plate.

A large number of enhancements is required, before the ALE-ANCF method can be applied in any of these practical applications. In general, a sophisticated algorithm that makes is possible for at node to move al the way through the modeled specimen is needed. This algorithm must be formed in a way such that no numerical singularities are encountered when one node is approaching another. In the numerical example shown here, the mesh was simple and consisted of only 4 elements. Further investigations must be made to clarify whether the ALE-ANCF method will work in a mesh with arbitrarily shaped elements. If the method is to be applied as a mesh refinement technique, some criteria is needed for determining when and which nodes should be moved and to which positions they should move. Furthermore, the criteria must be formulated in a way such that the solution is not compromised in other areas of the model. The application of the ALE-ANCF in crack propagation analysis is maybe the most interesting. This would allow for simulating realistic component failure in the multibody dynamics framework. However, this requires a model for how the node in the crack tip should move depending on the forces acting on the model. The model must also be made in a way such that the crack does not close again.

Besides the needed enhancements tied to the ALE-ANCF method, some more basic problems was noticed. Numerical difficulties were observed when the aspect ratio of the ALE-ANCF elements varied significantly from 1. These difficulties was noted at the beginning and the end of the simulation, were the numerical integrator used a smaller time step. Furthermore, it was problematic to find an appropriate model to use for validation of the ALE-ANCF method. Both results from traditional commercial finite element codes

and thin ANCF shell formulations was compared to the results from the dynamic simulation using the ALE-ANCF elements. The only successful validation was when the 36 d.o.f. element by Dmitrochenko and Pogorelov [2003] was used. This is remarkable since this element uses both the same kinematic and elastic description as the ALE-ANCF element presented here, while the other elements differs in some way. This could indicate a general difference in results obtained when using different formulation to analyze similar models could be expected. This will be investigated further in the next chapter.

Chapter 4

# Comparison of current ANCF thin shell formulations

To this point, several questions have been raised regarding the performance and comparability of current thin ANCF shell formulations. During the review of the element kinematics, several differences between the three described elements have been pointed out. Especially the difference in degree of gradient continuity of the various formulations is emphasized. During the validation of the ALE-ANCF element numerical problems was encountered when the mesh contained elements with large aspect ratios. This could indicate that the ANCF shell elements are sensitive to non-uniform mesh configurations. In addition, difficulties in finding a suitable model for the validation of ALE ANCF model could indicate that there may be a general difference between the 3 thin ANCF shell formulations. Another interesting fact was addressed in the introduction, namely that few studies have been conducted on thin ANCF shell elements in a curved configuration. In this chapter all these questions will be addressed. The chapter starts out with an investigation of how thin ANCF shell elements behaves in a curved configuration. Subsequently, the performance of the thin ANCF elements when used in a irregular mesh is studied. Finally, a general comparison of the 3 formulations treated in this report is carried out.

## 4.1 Kinematics of curved ANCF shell elements

In current thin rectangular ANCF shell elements, two different approaches have been used to create a set of interpolation shape functions. In the work of Dmitrochenko and Pogorelov [2003] products of cubic beam shape functions are used. This method is known as the crossed beam technique [Zienkiewicz and Taylor, 2000]. In the formulation presented by Dufva and Shabana [2005], the shape functions are based on an incomplete 4th order polynomial. Both of these methods and the choice of base functions used to establish the interpolation shape functions for elements addressed in this study are consistent with those known from Kirchhoff plate elements which are thoroughly discussed by Cook et al. [2002]. In this discussion several problematics regarding the kinematics of the Kirchoff plate formulation are mentioned. Shape functions based on the crossed beam technique lacks the ability to describe constant twist and the element shape functions derived from the incomplete quartic polynomial are known to have compatibility problems. Another concerning fact is that it is also mentioned that this type of element cannot be used to describe non-rectangular shapes. This concern is further manifested by the reality that engineering problems, in general, cannot be discretized entirely into rectangular shapes.

The lacking ability to describe non-rectangular shapes can be illustrated by discretization of a plane quarter hollow disc by 6 ANCF shell elements. This is depicted in Figure

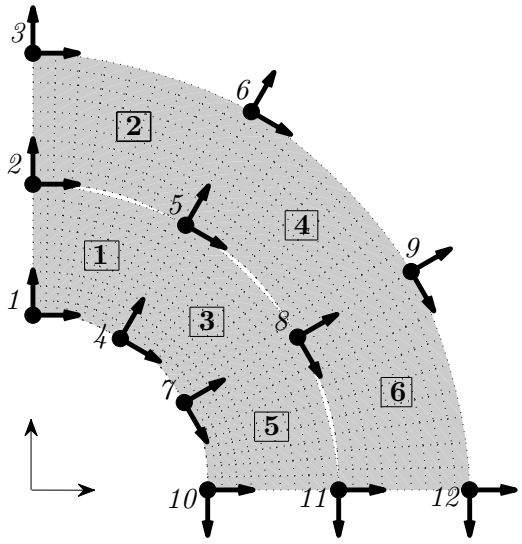


Figure 4.1: Hollow quarter disc with inner radius of 4 m and outer radius of 10 m discretized by 6 thin rectangular ANCF shell elements. The nodes are shown with their corresponding slope vectors. Node numbers are given in italic and element numbers are given in bold and in a box.

4.1. The elements are generated using the kinematic description of the 36 d.o.f. element by Dmitrochenko and Pogorelov [2003]. An equivalent figure can be obtained by using the kinematics of the 48 d.o.f. element or the 36 d.o.f. element by Dufva and Shabana [2005] thus leading to the same observations and conclusions. It is clear from Figure 4.1 that the elements are not covering the entire physical disc since there is a gap between adjacent curved element sides. This leads to a non-continuous description of the displacement field. It is noticeable that it is only between curved faces inter-element connectivity is lost, while the connectivity between straight sides are maintained. This suggests that the problem is confined to curved sides only. By closer inspection of the gap between element 3 and 4, further conclusions can be drawn. When comparing the element edges between nodes *5* and *8* to the segment of the circle they are meant to describe, it is seen that the edges lie on either side of the circular segment. See Figure 4.2a. Furthermore, by comparing the distances measured perpendicular from the true circle to the element edges it is seen that the gap is largest at the middle of the element span and it is nearly the same for the 2 elements but with opposite sign. See Figure 4.2b. The trend with the symmetric gap may not be the same in the case of arbitrary curved geometries.

Another interesting tendency can be spotted by closer inspection of the evaluation points used to plot the element edges. See Figure 4.2a. Here, the ticks on the curves displaying the element edges marks the position of the evenly distributed evaluation points obtained by interpolation of the nodal coordinates using the shape functions. The thin lines perpendicular to the true circle marks the equally spaced evaluation points on the circle. It is seen that the positions of the evaluation points on the elements edges are differing from the equally spaced points on the true circle. Furthermore, the spacing between the evaluation points on the elements are non-uniform. This same characteristic has previously been noted by Sanborn et al. [2011]. In their work this phenomena was labeled Curve Induced Distortion (CID) and they concluded that the phenomena causes membrane locking

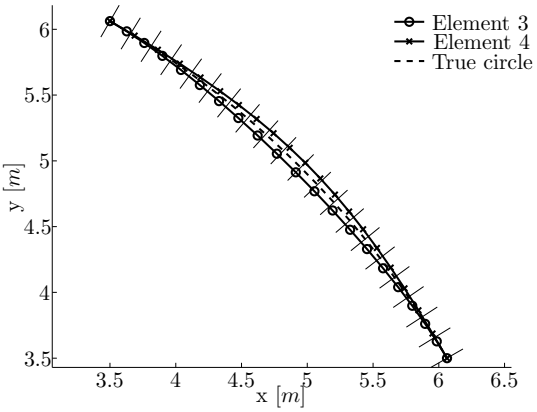


(a) Adjacent element edges for element 3 and 4 plotted together with the geometrically true circle they are trying to describe.

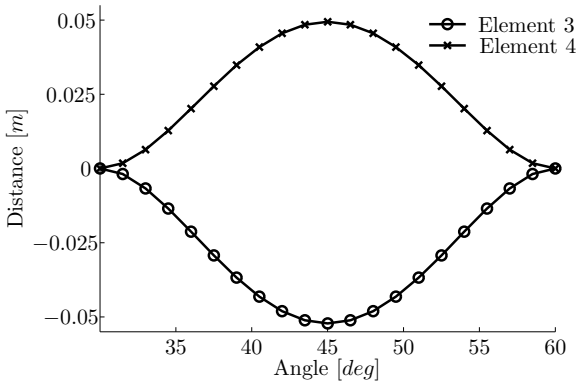


(b) Distance from curved element edge measured in the direction perpendicular to the true circle shown as a function of the span angle. A negative distance means that the edge lies on the inside of the true circle.

Figure 4.2: Gap between elements 3 and 4

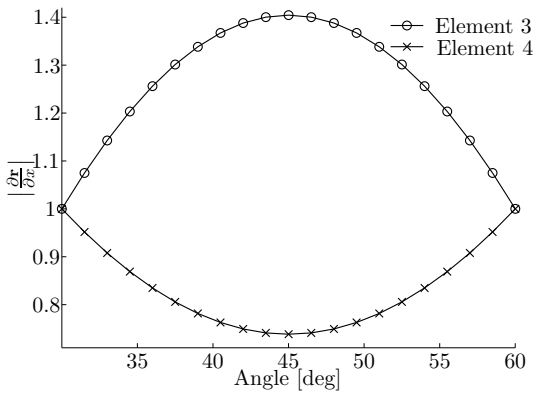


(a) Norm of the gradient vector $\frac{\partial \mathbf{r}}{\partial x}$.

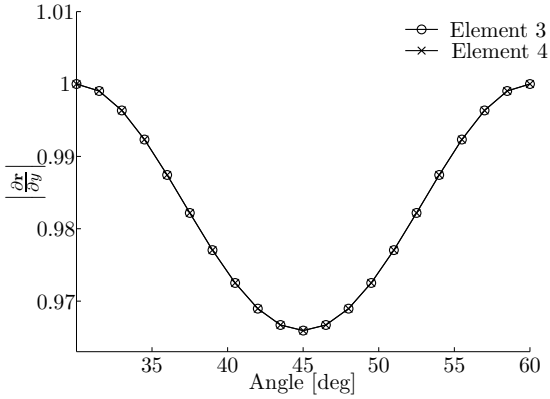


(b) Norm of the gradient vector $\frac{\partial \mathbf{r}}{\partial y}$.

Figure 4.3: Norm of gradient vectors at the element edges on the interface between elements 3 and 4 in their undeformed reference configuration.

in thin ANCF shell elements. CID occurs because of the use of polynomial based shape functions leads to a uneven distribution of the interpolated points on the described surface when it is deformed to a curved configuration. This means that gradients of the position field given in equation (2.1) are not unit vectors and the norm of the gradients vectors are non-constant if the position field is non-straight. A mathematical analysis of the topic is given in Farouki and Sakkalis [1991, 2007].

For the particular model used in this study the norm of the gradient vectors evaluated at the edges of element 3 and 4 in between nodes *5* and *8* are shown in Figure 4.3. The element strains is expressed in terms of the gradients by the Green-Lagrange strain tensor:

$$\epsilon_{\alpha\beta} = \frac{1}{2}\left(\frac{\partial \mathbf{r}}{\partial \alpha}^T \frac{\partial \mathbf{r}}{\partial \beta} - \delta_{\alpha\beta}\right) \tag{4.1}$$

where $\delta_{\alpha\beta}$ is the Kronecker delta. This means that a gradient norm larger that 1 corresponds to a state of tension and a norm less than 1 corresponds to compression. Using this it is

seen that, at the interface between element 3 and 4, element 3 is in tension and element 4 is in compression. See Figure 4.3a. Furthermore by inspection of the norm of the gradient perpendicular to the element interface, $\left|\frac{\partial \mathbf{r}}{\partial y}\right|$, it is seen that both elements are contracted to the same level, and the contraction is largest at the middle of the edges. See Figure 4.3b. These strains corresponds well to the elements depicted in Figure 4.1 where the elements are bent into curved shapes and contracting in radial direction thus creating the gap between the elements. This means that there are some significant strain levels in the elements in their undeformed reference configuration. It is believed that this bending behavior is partly due to the fact that the shape functions of the elements are derived for a shell in rectangular configuration. In this case the shell element is assumed to have a constant length and width at all evaluation points. When the element is used in a non-straight initial configuration the elements will have non-constant lengths and widths in their 'un-deformed' states.

It can be shown that the element configuration and inter-element connectivity is sensitive with respect to element parameters. For instance, changing the length of the slope vectors in the nodes will effect the contraction of a element. In the case of the hollow quarter circle used in this example, increasing the length of the $\frac{\partial \mathbf{r}}{\partial x}$ vector in nodes 5 and 8 will decrease the contraction in the y-direction of element 3. This will shift upper edge of this element outward and at some point it will match the actual circle it is trying to describe. The increase of the slope vector lengths at nodes 5 and 8 will also effect element 4. Here, it will increase the contraction of element 4 in the y-direction such that the gap between element 3 and 4 is maintained. Hereby it is concluded that as long as nodes are shared between curved elements, inter-element connectivity and correct geometrical description cannot be obtained by adjusting the length of the slope vectors at the nodes.

Other adjustable element parameters are the physical length and width of the elements. Normally these are considered constant for an entire element, also in the case of a curved elements. As previously mentioned, this assumption is considered to be partly responsible for the loss of inter-element connectivity when elements are used in a curved configuration. In the matter of fact it can be shown, that if the correct element lengths and widths corresponding to the actual geometry are used in the evaluation of its shape functions, the elements will resemble curved geometry in this example with only little loss of connectivity to its adjacent elements and the gradients of the position field are almost constant and unit vectors. Further studies must be made to clarify whether this technique of using unique element parameters at the evaluation points could solve the connectivity problem when applied arbitrary curved elements.

## 4.2 The influence non-uniform element size on model stiffness.

The finite element modeling of arbitrary real life structures often lead to a mesh where some elements have an aspect ratio that differs from unity. Especially, in cases where a fine mesh is used to enhance simulation results in areas of special interest, elements with larger aspect ratio are created in areas where a coarser mesh is sufficient. It is widely known that elements with large aspect ratio, hence $L_{max}/L_{min} \gg 1$, will affect the simulation result and furthermore abrupt changes in element size will lead to disturbances in the gradient field [Cook et al., 2002].

The sensitivity of current thin ANCF shell elements to varying aspect ratio and abrupt changing element size is investigated by studying the deflection of a simple structural

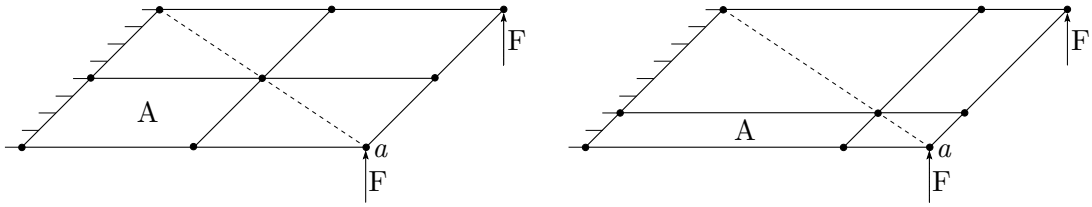


(a) Uniform element aspect ratio. (b) Non-uniform element aspect ratio.

Figure 4.4: Cantilever plate with transverse loading at corner points. The transverse deflection of point $a$ is monitored as the aspect ratio of element A is varied. The dashed line indicates the diagonal of the plate.

model subjected to static loading. The deflection is determined by calculating a set of nodal coordinates $\mathbf{q}$ yielding static equilibrium between an external applied force $\mathbf{Q}_f$ and the internal elastic forces $\mathbf{Q}_e$. The set of nodal coordinates is calculated using a iterative solution technique [Sopanen and Mikkola, 2003].

$$\mathbf{q}^{(n+1)} = \mathbf{q}^{(n)} - \left(\mathbf{K}_T^{(n)}\right)^{-1} \left(\mathbf{Q}_e^{(n)} - \mathbf{Q}_f^{(n)}\right) \tag{4.2}$$

In equation (4.2), $\mathbf{q}^{(n+1)}$ is the updated solution, $\mathbf{q}^{(n)}$ is the current solution, $\mathbf{K}_T^{(n)}$ is the tangent stiffness matrix at current iteration step and $\mathbf{Q}_e^{(n)}$ and $\mathbf{Q}_f^{(n)}$ are the elastic and external force vectors, respectively, at the current iteration step. The iteration loop is terminated when the internal and external forces are in equilibrium within some pre-defined error tolerance. The tangent stiffness matrix $\mathbf{K}_T^{(n)}$ is a highly non-linear function of the nodal coordinates and is calculated as:

$$\mathbf{K}_T^{(n)} = \frac{\partial \mathbf{Q}_e^{(n)}}{\partial \mathbf{q}^{(n)}} \tag{4.3}$$

In this investigation the tangent stiffness matrix is evaluated numerically using the finite difference method.

The model used to study the sensitivity of ANCF elements to varying aspect ratios is a simple cantilever plate. See Figure 4.4. The plate is modeled using 4 elements of equal size and aspect ratio $\mathrm{L_{max}/L_{min}} = 3$. A fixed boundary condition is applied by constraining the positions and slope vectors at the leftmost edge of the plate and a transverse load F applied at each of the two free corners. See Figure 4.4a. Subsequently, the mesh configuration is altered by shifting the center node toward the corner point $a$, keeping the center node on the plate diagonal and maintaining the rectangular element shapes. See Figure 4.4b. The transverse deflection is monitored at point a for each mesh configuration for comparison. Furthermore, deflections for the cantilever model is calculated using the commercial finite element solver Nastran using both CQUAD4 and CQUAD8 elements, which are 4 and 8 noded shell elements, respectively [MSC.Nastran, 2012]. The cantilever plate is assumed to have rectangular shape of size $L \times W \times t = 6\mathrm{m} \times 2\mathrm{m} \times 0.01\mathrm{m}$ made of a linear elastic isotropic material with a Young's modulus of $1 \times 10^7$ Pa and Poisson's ratio of 0.3. The force applied in each corner is 0.001 N. As the purpose of this investigation is to illustrate how the mesh configuration affects the model stiffness and not to evaluate the numerical precision of each formulation, the results have been normalized with respect to the deflection calculated with the uniform mesh. The normalized deflections are shown in Figure 4.5 as a function of the aspect ratio of element A, see Figure 4.4.

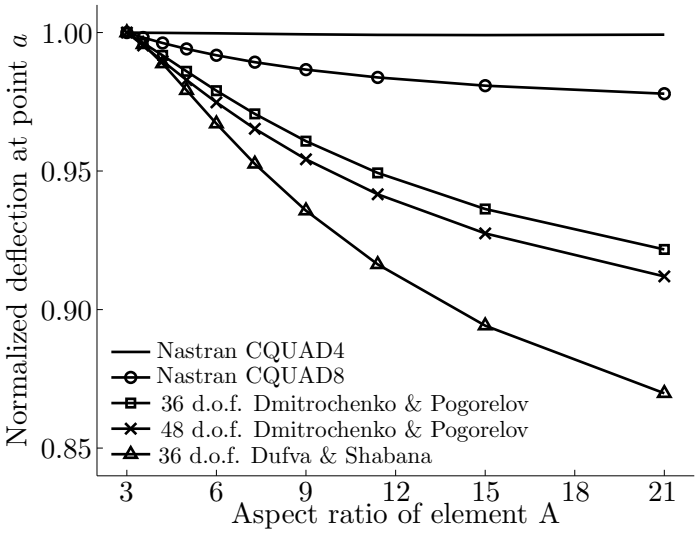


Figure 4.5: Normalized deflection of the corner of a cantilever plate as a function of element aspect ratio.

From Figure 4.5 it is seen that the simple 4 noded element CQUAD4 seems unaffected while the 8 noded CQUAD8 elements decreases slightly when increasing the aspect ratio of element A. The deflections of the ANCF based models diverges rapidly from the their calculated reference deflection when the mesh turns irregular. This indicates that the stiffness of the ANCF models is increasing more rapidly for an increasingly irregular mesh configuration, leading to an under-prediction of the actual deflection. It is also noticeable that the formulation by Dufva and Shabana [2005] seems more sensitive to the mesh configuration than the formulations by Dmitrochenko and Pogorelov [2003]. Furthermore, increased computational time was noticed for all the ANCF formulations with the increasing irregular mesh. Specifically, more iterations was needed in the solution process to acquire a converged solution.

In overall this simple study indicates that the ANCF based models appears more sensitive to irregular mesh configurations than conventional finite elements. Therefore it is suggested that ANCF based mesh containing irregular and/or elements with large aspect ratio should be used with caution and thorough convergence studies must be performed in order to obtain a good quality numerical model. Furthermore, the study has shown that there might be a general difference in results obtained using the formulations by Dufva and Shabana [2005] and Dmitrochenko and Pogorelov [2003], respectively, even though they use the same stiffness description. This behavior is investigated further in the next section.

## 4.3 Convergence comparison of thin ANCF shell elements

Both the validation of the ALE-ANCF element and the sensitivity study in the last section raises an interesting question, whether there is a general difference in results obtained using the 3 different thin ANCF shell element formulations. As mentioned earlier the 3 formulations uses the same stiffness description based on the Kirchhoff plate theory, but different approaches when defining the interpolation shape functions. Dufva and Shabana [2005] based their shape functions on an incomplete quartic polynomial to describe the

position $\mathbf{r}$.

$$\mathbf{r} = \mathbf{a}_1 + \mathbf{a}_2 x + \mathbf{a}_3 y + \mathbf{a}_4 x^2 + \mathbf{a}_5 xy + \mathbf{a}_6 y^2 + \mathbf{a}_7 x^3 + \mathbf{a}_8 y^2 x + \mathbf{a}_9 xy^2 + \mathbf{a}_{10} y^3 + \mathbf{a}_{11} x^3 y + \mathbf{a}_{12} xy^3 \tag{4.4}$$

where $\mathbf{a}_i$ are vectors of polynomial constants. It is seen that the displacement along any edge of the element will vary as a cubic which can be uniquely defined when using both the position and slope vectors as nodal degrees of freedom. See equation (2.5). The gradient field normal to any element edge will vary as a cubic polynomial, but since only two slope vectors normal to any element edge is utilized, this cubic polynomial is not unique. These two characteristics means that inter-element position continuity is ensured, but in general inter-element slope continuity is not, leading to a $C^0$ continuous description of the position field [Zienkiewicz and Taylor, 2000]. Dmitrochenko and Pogorelov [2003] used beam shape functions in combination with the crossed beam technique. The used beam shape functions are based on 1st order Hermitian polynomials which are inherently $C^1$ continuous. This means that the developed shape functions also will be $C^1$ continuous Zienkiewicz and Taylor [2000].

Since the bending strain energy is calculated based on the 2nd order partial derivatives, it is plausible that the degree of continuity of the overall displacement field could affect the response of models based on either of the two different approaches used to calculate the shape functions. To investigate this explanation the deflection of a plate subjected to transverse force $F$ acting in the center of the plate. A simply supported boundary condition is applied by fixing all displacements and slope vectors along the plate edges at the boundary nodes. The plate is assumed to have side lengths of 1 m, a thickness of 0.01 m, a Young's modulus of $1 \times 10^7$ Pa and a Poisson's ratio of 0.3. The center point deflection is calculated for several mesh sizes using all 3 ANCF shell formulations for 3 load cases: F = 0.1 N, 1.0 N and 10 N. The deflections are calculated using the same approach as described in the previous section. The results are compared to corresponding results obtained using the commercial finite element solver Nastran. Here the same model is analyzed using CQUAD8 elements and solved using the implicit non-linear SOL400 solution sequence [MSC.Nastran, 2012].

The results from all three ANCF models are shown in Figure 4.6 together with the results from Nastran. The results clearly show that there is a general difference between the formulations since the elements by Dmitrochenko & Pogorelov converge to a lower deflection than the element by Dufva & Shabana. Furthermore, in all three load cases the formulation by Dufva & Shabana converge to a result comparable to that obtained by the conventional CQUAD8 elements. It is also noticeable that in the load case where F = 0.1 N, the formulation by Dufva & Shabana is heavily over predicting deflection for a coarse mesh. See Figure 4.6a. This trend seems to be waning as the load increases, and finally converging in the same pattern as the formulation by Dmitrochenko & Pogorelov at F = 10 N. See Figure 4.6c. Another interesting tendency, is that 48 d.o.f. element perform significantly better than the 36 d.o.f. element by Dmitrochenko & Pogorelov. Especially in the two load cases with $F = -0.1$ N and $F = -1.0$ N where the 48 d.o.f. element converges to a result closer to the results from both Nastran and the 36 d.o.f. element by Dufva & Shabana. This suggests that important polynomial terms are excluded from the shape functions when omitting the 2nd order slope vectors from the generalized coordinates. In general, the ANCF models converge much slower than the conventional CQUAD8 element models meaning that a significantly higher number of elements are needed to obtain a converged solution.

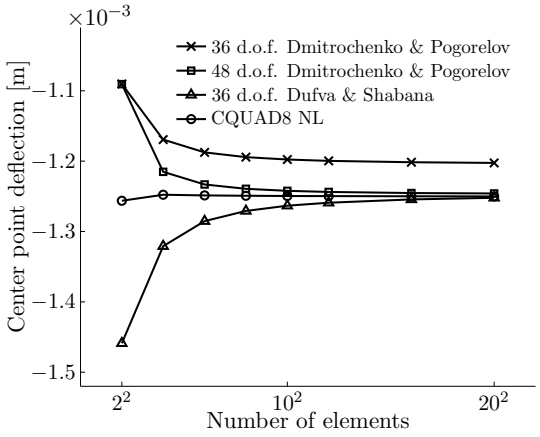


(a) Center point deflection when F = −0.1 N.

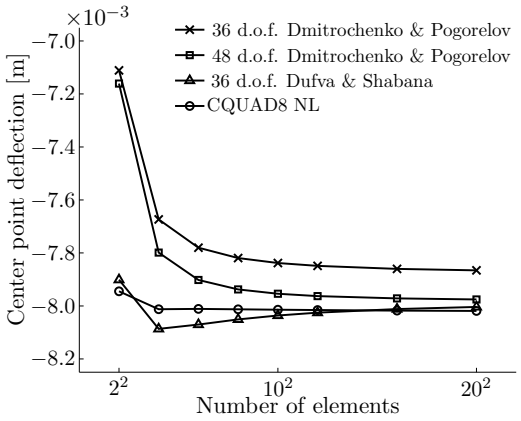


(b) Center point deflection when F = −1.0 N.

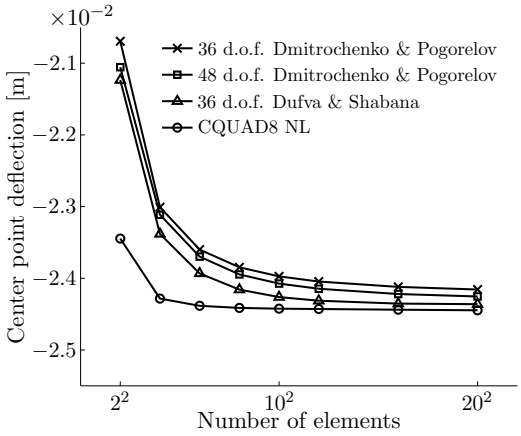


(c) Center point deflection when F = −10 N.

Figure 4.6: Deflections measured at the center point of the simply supported square plate for varying loads

## 4.4 Discussion

The three simple investigations presented in this chapter have shown that thin ANCF shell elements have some issues which must be addressed before they can be used as an analysis tool in practical applications. The investigation of the element behavior in curved configurations showed that curved geometry cannot described accurately when discretized by current thin shell formulations. However, this study has not clarified what influence this lack of element compatibility will have on numerical results. Further studies is needed to investigate what influence the element gaps will have on analysis results, and to determine if the problem will be become insignificant if an increased number of elements is used.

The investigation of the shell elements sensitivity to non-uniform mesh configuration showed that the ANCF shell element performed considerably worse with meshes containing elements with large aspect ratios. Both decreasing solution accuracy and increased computational time was noted with growing element aspect ratio. This effedt needs consideration when building finite element meshes consisting of thin ANCF shell elements. However the elements formulated by Dmitrochenko & Pogorelov seemed less sensitive to the irregular mesh than the element by Dufva & Shabana. This could indicate that the shape functions

based on Hermite polynomials are less sensitive to high element aspect ratios. It was also remarkable, that the lower order conventional finite elements appears much less sensitive to the non-uniform mesh than the higher order ANCF elements. This indicates that the conventional finite elements are more flexible and can be used with less considerations regarding mesh quality.

A general comparison of the three element formulations with a traditional large displacement finite element solution showed that the ANCF elements are converging much slower and to a less deflected solution than the traditional finite elements. This could indicate that the ANCF elements are prone to locking. This have in the matter of fact been reported in the paper by Sanborn et al. [2011]. In the three different load cases presented here, it is the 36 d.o.f. element by Dufva & Shabana that produces converged results that are closest to the solutions obtained using the conventional finite elements. Unfortunately, this element has the disadvantage that it underestimates the deflection significantly when the model is dominated by bending deformations. This trend may be due to the element uses shape functions that are only $C^0$ continuous. In overall, this comparison is inadequate and further comparisons with e.g. analytical large displacement solutions are necessary to determine whether the thin ANCF shell elements are exhibit poor precision in general. However, both the sensitivity and the convergence study have shown that the element continuity degree will have an influence on the simulation results. Though, it was surprising that it was the element based on the $C^0$ continuous shape functions which gave the best results. This is due to the fact that $C^1$ continuous shape functions have been mentioned in section 2.1 as a requirement when calculating the element stiffness based on the curvature of the position field. This suggests that it may be admissible to relax this requirement when developing new ANCF shell finite elements.

Chapter 5

# Conclusion

In this report, several aspects of thin ANCF shell elements have been addressed. A thorough literature review has covered the currently available elements and pointed out the differences between the methods used to describe the element kinematics. Subsequently, the equations of motion was derived in a general way. During the derivation, several of the advantages that make ANCF attractive for implementation in multibody dynamics was emphasized. These are the simple kinematic description and the constant mass matrix.

A novel ALE-ANCF shell element that combines the ANCF with aspects from the ALE formulation was briefly reviewed. Using this combination, ALE-ANCF elements are able to change the mesh configuration dynamically during a simulation forward in time. Despite the fact that the formulation still requires some substantial enhancements, several possible practical applications was mentioned where the ALE-ANCF could be beneficial. Especially the possibility to use the formulation as a tool to analyze crack propagation in the multibody dynamics environment is something which calls for further investigation.

The behavior of thin ANCF shell elements used in a curved configuration was studied. This study concluded that current elements lacks the ability to represent curved structures without loss of inter-element displacement continuity. The consequence of this still needs to be addressed and evaluated. The performance of the thin ANCF shell formulations have been studied both when used in a non-uniform mesh and in a more general case. The investigation showed that the ANCF shell elements are more sensitive to irregular meshes when compared to traditional finite elements. This should be kept in mind when creating a finite element mesh containing ANCF shell elements. The general comparison of the ANCF elements pointed out that they both converge slowly and to quite different results, when compared to traditional finite element solutions.

Based on the conclusions from the comparison of the current thin ANCF shell elements, it is not recommended in a design process to use any of the formulations in the form they are presented here. This is due to the lacking ability to describe arbitrary real life geometries, poor precision, and slow convergence characteristics. Furthermore, the ALE-ANCF element should also be used with care, since it is based on the current thin ANCF elements. However, with further research and development the thin ANCF shell elements may well become an valuable tool in the future design processes.

Chapter 6

# Outlook and future work

As mentioned in the conclusion, the thin ANCF shell elements have a great potential and it would be unfortunate not to explore this. With further refinement, it could be possible to analyze large, flexible complex geometry structures with the intent of designing better products, e.g. larger and lighter wind turbine blades or aircraft wings.

The remaining part of this PhD study is dedicated to the continuous development of the ANCF and in particular of thin ANCF shell elements. The first point of interest is clearly the kinematic description. It must be verified whether or not the loss of element compatibility, when used in a curved configuration, can be ignored. If not, a new and better kinematic description must be applied. One possible improvement is already mentioned in section 4.1. The use of unique element parameters that depends on the elements initial reference configuration. This approach has been noted to relax the problem of element gaps in the simple plane example addressed in section 4.1. Further investigations are needed to verify whether this solution also could be applied in arbitrary curved structures. Other possible solutions could be to add nodes to the elements and/or use other combinations of slope vectors. This could be combined with other and more sophisticated basis interpolation functions such as Bezier curves or non-uniform rational B-splines (NURBS) [Piegl and Tiller, 1997].

Another aspect that could be desirable to address is the stiffness description. So far, it has been the simple Kirchhoff shell theory in combination with the Green-Lagrange strain tensor which has been used. It could be interesting to investigate the possibility of applying other and maybe more suitable plate and shell theories. This approach of using advanced structural mechanics theories has proven useful in the development of the ANCF beam elements. Hence, it is also assumed that this could improve thin ANCF shell elements.

# Bibliography


Cook, R. D., Malkus, D. S., Plesha, M. E., and Witt, R. J. (2002). *Concepts and applications of finite element analysis*. John Wiley & Sons, Hoboken, $4^{th}$ edition.

Dmitrochenko, O. and Mikkola, A. (2008). Two simple triangular plate elements based on the absolute nodal coordinate formulation. *Journal of Computational and Nonlinear Dynamics*. DOI 10.1115/1.2960479.

Dmitrochenko, O. and Pogorelov, D. (2003). Generalization of plate finite elements for absolute nodal coordinate formulation. *Multibody System Dynamics*, 10:17–43.

Donea, J., Huerta, A., Ponthot, J.-P., and Rodríguez-Ferran, A. (2004). *Arbitrary Lagrangian-Eulerian methods*, volume 1: Fundamentals of *Encyclopedia of Computational Mechanics*, chapter 14. John Wiley & Sons, Ltd.

Dufva, K. and Shabana, A. A. (2005). Analysis of thin plate structures using the absolute nodal coordinate formulation. *Journal of Multi-Body Dynamics*, 219:345–355.

Farouki, R. T. and Sakkalis, T. (1991). Real rational curves are not 'unit speed'. *Computer Aided Geometric Design*, 8:151–157.

Farouki, R. T. and Sakkalis, T. (2007). Rational space curves are not 'unit speed'. *Computer Aided Geometric Design*, 24:238–240.

García-Vallejo, D., Mikkola, A., and Escalona, J. L. (2007). A new locking-free shear deformable finite element based on absolute nodal coordinates. *Nonlinear Dynamics*, 50:249–264.

Gerstmayr, J. and Shabana, A. A. (2005). Analysis of thin beams and cables using the absolute nodal co-ordinate formulation. *Nonlinear Dynamics*, 45:109–130.

Gerstmayr, J., Sugiyama, H., and Mikkola, A. (2012). An overview on the developments of the absolute nodal coordinate formulation. *Proceedings of the 2nd Joint International Conference on Multibody System Dynamics*.

Haug, E. J. (1989). *Computer Aided Kinematics and Dynamics of Mechanical Systems. Volume 1: Basic Methods*. Allyn and Bacon, Boston.

Hong, D. and Ren, G. (2011). A modeling of sliding joint on one-dimensional flexible medium. *Multibody System Dynamics*, 26:91–106.

Hong, D., Tant, J., and Ren, G. (2011). Dynamic modeling of mass-flowing linear medium with large amplitude displacement and rotation. *Journal of Fluids and Structures*, 27:1137–1148.

Hyldahl, P., Mikkola, A., and Balling, O. (2013). A thin plate element based on the combined arbitrary lagrange-euler and absolute nodal coordinate formulations. *Journal of Multi-body Dynamics*. DOI 10.1177/1464419313480351.

Lee, J.-H. and Park, T.-W. (2013). Development of a three-dimensional catenary model using cable elements based on absolute nodal coordinate formulation. *Journal of Mechanical Science and Technology*, 26:3933–3941.

Matikainen, M. and Mikkola, A. (2005). Improved description of elastic forces for the absolute nodal coordinate based plate element. In *Proceedings of the ASME 2005 International Design Engineering Technical Conferences & Computers and Information in Engineering Conference*, pages 1277–1283, Long Beach, California USA. ASME.

Mikkola, A. and Shabana, A. A. (2003). A non-incremental finite element procedure for the analysis of large deformation of plates and shells in mechanical system application. *Multibody System Dynamics*, 9:283–309.

Morley, L. S. D. (1971). The constant-moment plate bending element. *Journal of Strain Analysis*, 6:20–24.

MSC.Nastran (2012). *Quick Reference Guide, MSC.Software Corporation*.

Nachbagauer, K., Pechstein, A. S., Irschik, H., and Gerstmayr, J. (2011). A new locking-free formulation for planar, shear deformable, linear and quadratic beam finite elements based on the absolute nodal coordinate formulation. *Multibody System Dynamics*, 26:245–263.

Nikravesh, P. E. (1988). *Computer Aided Analysis of Mechanical Systems*. Prentice Hall, Englewood Cliffs.

Omar, M. A., Shabana, A. A., Mikkola, A., Loh, W.-Y., and Basch, R. (2004). Multibody system modeling of leaf springs. *Journal of Vibration and Control*, 11:1601–1638.

Piegl, L. and Tiller, W. (1997). *The NURBS Book*. Springer Verlag, Berlin, $2^{nd}$ edition.

Sanborn, G. G., Choi, J., and Choi, J. H. (2011). Curve-induced distortion of polynomial space curves, flat-mapped extension modeling, and their impact on ancf thin-plate finite elements. *Multibody System Dynamics*, 26:191–211.

Schiehlen, W. (1997). Multibody system dynamics: Roots and perspectives. *Multibody System Dynamics*, 1:149–188.

Schreurs, P., Veldpas, F., and Brekelmans, W. (1986). Simulation of forming processes, using the arbitrary eulerian-lagrangian formulation. *Computer Methods in Applied Mechanics and Engineering*, 58:19–36.

Seo, J.-H., Kim, S.-W., Jung, I.-H., Park, T.-W., Mok, J.-Y., Kim, Y.-G., and Chai, J.-B. (2006). Dynamic analysis of a pantograph–catenary system using absolute nodal coordinates. *Vehicle System Dynamics*, 44:615–630.

Shabana, A. A. (1996). An absolute nodal coordinate formulation for the large rotation and deformation analysis of flexible bodies. Technical Report No. MBS96-1-UIC, Department of Mechanical Engineering, University of Illinois at Chicago.

Shabana, A. A. (1997a). Definition of the slopes and the finite element absolute nodal coordinate formulation. *Multibody System Dynamics*, 1:339–348.

Shabana, A. A. (1997b). Flexible multibody dynamics: Review of past and recent developments. *Multibody System Dynamics*, 1:189–222.

Shabana, A. A. (2005). *Dynamics of Multibody Systems*. Cambridge University Press, New York, $3^{rd}$ edition.

Shabana, A. A. and Christensen, A. P. (1997). Three dimensional absolute nodal coordinate formulation: Plate problem. *International Journal for Numerical Methods in Engineering*, 40:2775–2790.

Shabana, A. A. and Yakoub, R. (2001). Three dimensional absolute nodal coordinate formulation for beam theory: Theory. *Journal of Mechanical Design*, 123:606–613.

Sopanen, J. and Mikkola, A. (2003). Description of elastic forces in absolute nodal coordinate formulation. *Nonlinear Dynamics*, 34:53–74.

Specht, B. (1988). Modifid shape functions for the three-noded plate bending element passing the patch test. *International Journal for Numerical Methods in Engineering*, 26:705–715.

Sugiyama, H. and Suda, Y. (2009). Multibody system modeling of leaf springs. *Journal of Vibration and Control*, 223:211–219.

Timoshenko, S. P. and Woinowsky-Krieger, S. (1959). *Theory of Plates and Shells*. McGraw-Hill Book Company, New York, $2^{nd}$ edition.

Wasfy, T. M. and Noor, A. K. (2003). Computational strategies for flexible multibody systems. *Applied Mechanics Review*, 56:553–613.

Yang, C. J., Hong, D. F., Ren, G. X., and Zhao, Z. H. (2013). Cable installation simulation by using a multibody dynamic model. *Multibody System Dynamics*. DOI 10.1007/s11044-013-9364-9.

Zienkiewicz, O. C. and Taylor, R. L. (2000). *The Finite Element Method For Solid & Structural Mechanics*. Butterworth-Heineman, Oxford, $5^{th}$ edition.

Zienkiewicz, O. C., Taylor, R. L., and Zhu, J. (2000). *The Finite Element Method Its Basis & Fundamentals*. Butterworth-Heineman, Oxford, $5^{th}$ edition.

Appendix **A**

# Shape functions based on the crossed beam technique

This appendix contains the derivation of a set of interpolation shape functions for a 4 noded, 48 d.o.f. rectangular ANCF plate element. The shape functions are derived using products of beam shape functions known as the crossed beam technique, see [Zienkiewicz and Taylor, 2000, Section 11.14].

A set of beam shape functions $\mathbf{S}$ based on a $1st$ order Hermite polynomial is expressed as:

$$\mathbf{S}(\xi) = [S_1(\xi) \quad S_2(\xi) \quad S_3(\xi) \quad S_4(\xi)] \otimes \mathbf{I}_{3\times 3} \tag{A.1}$$

where

$$\begin{aligned} S_1(\xi) &= 1 - 3\xi^2 + 2\xi^3 \\ S_2(\xi) &= L\left(\xi - 2\xi^2 + \xi^3\right) \\ S_3(\xi) &= 3\xi^2 - 2\xi^3 \\ S_4(\xi) &= L\left(-\xi^2 + \xi^3\right) \end{aligned} \tag{A.2}$$

Here; L is the element length and $\xi = x/L$ is an isoparametric mapping parameter ranging $0 \leq \xi \leq 1$. These shape functions will be used to interpolate in the $x$-direction in the plate element. A similar set of shape functions $\mathbf{P}$ to interpolate in the $y$-direction is obtained by substituting $\xi$ and $L$ in equation (A.2) with $\eta = y/W$ and $W$ as follows:

$$\mathbf{P}(\eta) = [P_1(\eta) \quad P_2(\eta) \quad P_3(\eta) \quad P_4(\eta)] \otimes \mathbf{I}_{3\times 3} \tag{A.3}$$

where

$$\begin{aligned} P_1(\eta) &= 1 - 3\eta^2 + 2\eta^3 \\ P_2(\eta) &= W\left(\eta - 2\eta^2 + \eta^3\right) \\ P_3(\eta) &= 3\eta^2 - 2\eta^3 \\ P_4(\eta) &= W\left(-\eta^2 + \eta^3\right) \end{aligned} \tag{A.4}$$

$W$ denotes the element width.

The shape function matrix of the plate element $\mathbf{N}$ will be a $3 \times 48$ matrix containing 16 unique shape functions:

$$\mathbf{N}(\xi,\eta) = [N_1(\xi,\eta) \quad N_2(\xi,\eta) \quad \ldots \quad N_{15}(\xi,\eta) \quad N_{16}(\xi,\eta)] \otimes \mathbf{I}_{3\times 3} \tag{A.5}$$

The 4 plate element shape functions associated to node 1 in the plate element are calculated as:

$$\begin{aligned} N_1(\xi,\eta) &= S_1(\xi)P_1(\eta) \\ N_2(\xi,\eta) &= S_2(\xi)P_1(\eta) \\ N_3(\xi,\eta) &= S_1(\xi)P_2(\eta) \\ N_4(\xi,\eta) &= S_2(\xi)P_2(\eta) \end{aligned} \tag{A.6}$$

These shape functions correspond to the nodal coordinates $\mathbf{r}_1$, $\frac{\partial \mathbf{r}_1}{\partial x}$, $\frac{\partial \mathbf{r}_1}{\partial y}$, and $\frac{\partial^2 \mathbf{r}_1}{\partial x \partial y}$, respectively.

The 4 shape functions associated to node 2 in the plate element are calculated as:

$$\begin{aligned} N_5(\xi,\eta) &= S_3(\xi)P_1(\eta) \\ N_6(\xi,\eta) &= S_4(\xi)P_1(\eta) \\ N_7(\xi,\eta) &= S_3(\xi)P_2(\eta) \\ N_8(\xi,\eta) &= S_4(\xi)P_2(\eta) \end{aligned} \tag{A.7}$$

These shape functions correspond to the nodal coordinates $\mathbf{r}_2$, $\frac{\partial \mathbf{r}_2}{\partial x}$, $\frac{\partial \mathbf{r}_2}{\partial y}$, and $\frac{\partial^2 \mathbf{r}_2}{\partial x \partial y}$, respectively.

The 4 shape functions associated to node 3 in the plate element are calculated as:

$$\begin{aligned} N_9(\xi,\eta) &= S_3(\xi)P_3(\eta) \\ N_{10}(\xi,\eta) &= S_4(\xi)P_3(\eta) \\ N_{11}(\xi,\eta) &= S_3(\xi)P_4(\eta) \\ N_{12}(\xi,\eta) &= S_4(\xi)P_4(\eta) \end{aligned} \tag{A.8}$$

These shape functions correspond to the nodal coordinates $\mathbf{r}_3$, $\frac{\partial \mathbf{r}_3}{\partial x}$, $\frac{\partial \mathbf{r}_3}{\partial y}$, and $\frac{\partial^2 \mathbf{r}_3}{\partial x \partial y}$, respectively.

The 4 shape functions associated to node 4 in the plate element are calculated as:

$$\begin{aligned} N_{13}(\xi,\eta) &= S_1(\xi)P_3(\eta) \\ N_{14}(\xi,\eta) &= S_2(\xi)P_3(\eta) \\ N_{15}(\xi,\eta) &= S_1(\xi)P_4(\eta) \\ N_{16}(\xi,\eta) &= S_2(\xi)P_4(\eta) \end{aligned} \tag{A.9}$$

These shape functions correspond to the nodal coordinates $\mathbf{r}_4$, $\frac{\partial \mathbf{r}_4}{\partial x}$, $\frac{\partial \mathbf{r}_4}{\partial y}$, and $\frac{\partial^2 \mathbf{r}_4}{\partial x \partial y}$, respectively.

By calculation and reduction, the 16 individual shape functions are expressed as:

$$
\begin{aligned}
N_1 &= (2\xi+1)(-1+\xi)^2(2\eta+1)(-1+\eta)^2 \\
N_2 &= L\xi(-1+\xi)^2(2\eta+1)(-1+\eta)^2 \\
N_3 &= (2\xi+1)(-1+\xi)^2 W\eta(-1+\eta)^2 \\
N_4 &= L\xi(-1+\xi)^2 W\eta(-1+\eta)^2 \\
N_5 &= -\xi^2(-3+2\xi)(2\eta+1)(-1+\eta)^2 \\
N_6 &= L\xi^2(-1+\xi)(2\eta+1)(-1+\eta)^2 \\
N_7 &= -\xi^2(-3+2\xi)W\eta(-1+\eta)^2 \\
N_8 &= L\xi^2(-1+\xi)W\eta(-1+\eta)^2 \\
N_9 &= \xi^2(-3+2\xi)\eta^2(-3+2\eta) \\
N_{10} &= -L\xi^2(-1+\xi)\eta^2(-3+2\eta) \\
N_{11} &= -\xi^2(-3+2\xi)W\eta^2(-1+\eta) \\
N_{12} &= L\xi^2(-1+\xi)W\eta^2(-1+\eta) \\
N_{13} &= -(2\xi+1)(-1+\xi)^2\eta^2(-3+2\eta) \\
N_{14} &= -L\xi(-1+\xi)^2\eta^2(-3+2\eta) \\
N_{15} &= (2\xi+1)(-1+\xi)^2 W\eta^2(-1+\eta) \\
N_{16} &= L\xi(-1+\xi)^2 W\eta^2(-1+\eta)
\end{aligned}
\tag{A.10}
$$

Appendix **B**

# Shape functions based on a polynomial ekspasion

This appendix contains the derivation of a set of interpolation shape functions for a 4 noded, 36 d.o.f. rectangular ANCF plate element. The shape functions are derived using an assumed displacement field based on a polynomial expansion, see [Zienkiewicz et al., 2000; Cook et al., 2002]. For a Kirchhoff type plate element, the polynomial terms are taken from an incomplete quartic polynomial and arranged in a row vector $\mathbf{X}$:

$$\mathbf{X} = \begin{bmatrix} 1 & x & y & x^2 & xy & y^2 & x^3 & x^2y & xy^2 & y^3 & x^3y & xy^3 \end{bmatrix} \tag{B.1}$$

The derivatives of $\mathbf{X}$ with respect to the local element coordinates $x$ and $y$ are given by:

$$\begin{aligned} \frac{\partial \mathbf{X}}{\partial x} &= \begin{bmatrix} 0 & 1 & 0 & 2x & y & 0 & 3x^2 & 2xy & y^2 & 0 & 3x^2y & y^3 \end{bmatrix} \\ \frac{\partial \mathbf{X}}{\partial y} &= \begin{bmatrix} 0 & 0 & 1 & 0 & x & 2y & 0 & x^2 & 2xy & 3y^2 & x^3 & 3xy^2 \end{bmatrix} \end{aligned} \tag{B.2}$$

The shape function matrix of the plate element $\mathbf{N}$ will be a $3 \times 36$ matrix containing 12 unique shape functions:

$$\mathbf{N}(\xi, \eta) = \begin{bmatrix} N_1(\xi,\eta) & N_2(\xi,\eta) & \dots & N_{11}(\xi,\eta) & N_{12}(\xi,\eta) \end{bmatrix} \otimes \mathbf{I}_{3\times 3} \tag{B.3}$$

The 12 unique shape function matrix $\mathbf{N}$ is calculated using the following relationship:

$$\mathbf{N} = \mathbf{X}\mathbf{A}^{-1} \tag{B.4}$$

$\mathbf{A}$ is a square $12 \times 12$ matrix and each row are $\mathbf{X}$, $\frac{\partial \mathbf{X}}{\partial x}$, and $\frac{\partial \mathbf{X}}{\partial y}$ evaluated at each node:

$$\mathbf{A} = \begin{bmatrix} \mathbf{X}|_{x=0,y=0} & \left.\frac{\partial \mathbf{X}}{\partial x}\right|_{x=0,y=0} & \left.\frac{\partial \mathbf{X}}{\partial y}\right|_{x=0,y=0} \\ \mathbf{X}|_{x=L,y=0} & \left.\frac{\partial \mathbf{X}}{\partial x}\right|_{x=L,y=0} & \left.\frac{\partial \mathbf{X}}{\partial y}\right|_{x=L,y=0} \\ \mathbf{X}|_{x=L,y=W} & \left.\frac{\partial \mathbf{X}}{\partial x}\right|_{x=L,y=W} & \left.\frac{\partial \mathbf{X}}{\partial y}\right|_{x=L,y=W} \\ \mathbf{X}|_{x=0,y=W} & \left.\frac{\partial \mathbf{X}}{\partial x}\right|_{x=0,y=W} & \left.\frac{\partial \mathbf{X}}{\partial y}\right|_{x=0,y=W} \end{bmatrix}^T \tag{B.5}$$

Note that the transpose signs over each term inside square brackets has been omitted. When the terms are evaluated the **A** matrix takes the form:

$$\mathbf{A} = \begin{bmatrix}
1 & 0 & 0 & 0 & 0 & 0 & 0 & 0 & 0 & 0 & 0 & 0 \\
0 & 1 & 0 & 0 & 0 & 0 & 0 & 0 & 0 & 0 & 0 & 0 \\
0 & 0 & 1 & 0 & 0 & 0 & 0 & 0 & 0 & 0 & 0 & 0 \\
1 & l & 0 & l^2 & 0 & 0 & l^3 & 0 & 0 & 0 & 0 & 0 \\
0 & 1 & 0 & 2\,l & 0 & 0 & 3\,l^2 & 0 & 0 & 0 & 0 & 0 \\
0 & 0 & 1 & 0 & l & 0 & 0 & l^2 & 0 & 0 & l^3 & 0 \\
1 & l & w & l^2 & lw & w^2 & l^3 & l^2w & lw^2 & w^3 & l^3w & lw^3 \\
0 & 1 & 0 & 2\,l & w & 0 & 3\,l^2 & 2\,lw & w^2 & 0 & 3\,l^2w & w^3 \\
0 & 0 & 1 & 0 & l & 2\,w & 0 & l^2 & 2\,lw & 3\,w^2 & l^3 & 3\,lw^2 \\
1 & 0 & w & 0 & 0 & w^2 & 0 & 0 & 0 & w^3 & 0 & 0 \\
0 & 1 & 0 & 0 & w & 0 & 0 & 0 & w^2 & 0 & 0 & w^3 \\
0 & 0 & 1 & 0 & 0 & 2\,w & 0 & 0 & 0 & 3\,w^2 & 0 & 0
\end{bmatrix} \tag{B.6}$$

When inserting equation (B.1) and (B.6) into equation (B.4), the 12 individual shape functions are calculated:

$$\begin{aligned}
N_1 &= -(-1+\xi)(-1+\eta)(2\eta^2-\eta+2\xi^2-\xi-1) \\
N_2 &= -\xi L(-1+\xi)^2(-1+\eta) \\
N_3 &= -\eta W(-1+\eta)^2(-1+\xi) \\
N_4 &= \xi(-1+\eta)(2\eta^2-\eta-3\xi+2\xi^2) \\
N_5 &= -\xi^2 L(-1+\xi)(-1+\eta) \\
N_6 &= \eta W(-1+\eta)^2\xi \\
N_7 &= -\eta\xi(-3\xi+2\xi^2+1-3\eta+2\eta^2) \\
N_8 &= \eta\xi^2 L(-1+\xi) \\
N_9 &= \eta^2 W(-1+\eta)\xi \\
N_{10} &= \eta(-1+\xi)(2\xi^2-\xi+2\eta^2-3\eta) \\
N_{11} &= \eta\xi L(-1+\xi)^2 \\
N_{12} &= -\eta^2 W(-1+\xi)(-1+\eta)
\end{aligned} \tag{B.7}$$

# Hyldahl, Per: Large Displacement Analysis of Shell Structures using the Absolute Nodal Coordinate Formulation, 2013

**Department of Engineering**
Aarhus University
Edison, Finlandsgade 22
8200 Aarhus N
Denmark

Tel.: +45 4189 3000